

Banner appropriate to article type will appear here in typeset article

# Nonlinear electrohydrodynamics of a surfactant-laden leaky dielectric drop

Michael A. McDougall <sup>1</sup>†, Stephen K. Wilson  <sup>2,1</sup>‡ and Debasish Das  <sup>1</sup>¶

<sup>1</sup>Department of Mathematics and Statistics, University of Strathclyde, Livingstone Tower, 26 Richmond Street, Glasgow G1 1XH, United Kingdom

<sup>2</sup>Department of Mathematical Sciences, University of Bath, Claverton Down, Bath BA2 7AY, United Kingdom

(Received xx; revised xx; accepted xx)

A nonlinear three-dimensional small-deformation theory is presented for a leaky dielectric drop coated with a dilute monolayer of insoluble apolar surfactant and subjected to a uniform DC electric field. The theory is developed within the framework of the Taylor–Melcher leaky dielectric model, and builds on previous work by retaining surface charge convection in the charge conservation equation. Solving the problem in three dimensions and retaining charge convection allows us to capture the transition to Quincke rotation, a symmetry breaking instability wherein a drop begins rotating at a steady angular velocity when the applied electric field strength exceeds a critical value. We derive a system of coupled nonlinear ordinary differential equations for the drop shape, dipole moment, and surfactant distribution, which we solve numerically. We discuss the combined effects of charge convection and surfactant in the Taylor regime – in which the field strength is too weak to induce Quincke rotation and the drop adopts an axisymmetric spheroidal shape. In the Quincke regime, we find that the presence of a weakly-diffusing surfactant results in a lower critical electric field than that for a drop with uniform surfactant coverage. Varying the elasticity number, which quantifies the variation of the surface tension as a function of the surfactant concentration, can either increase or decrease the critical field strength depending on the diffusivity of the surfactant. Additionally, we find that the experimentally observed hysteresis in the angular velocity of the drop can disappear when surfactant diffusion is sufficiently weak.

**Key words:** Authors should not enter keywords on the manuscript, as these must be chosen by the author during the online submission process and will then be added during the typesetting process (see [Keyword PDF](#) for the full list). Other classifications will be added at the same time.

---

**MSC Codes** (*Optional*) Please enter your MSC Codes here

† Email address for correspondence: michael.mcdougall@strath.ac.uk

‡ sw3197@bath.ac.uk

¶ debasish.das@strath.ac.uk

## 1. Introduction

Surfactants (surface active agents) are a class of chemical compounds that reduce the surface tension between a liquid and a second medium, and are widely employed across several industries for their useful interfacial properties. Among their uses are emulsification, often exploited for food processing (Kralova & Sjöblom 2009); wetting, used to develop improved agricultural chemicals like pesticides and fertilisers (Kovalchuk & Simmons 2021); foaming, used to develop a range of personal care products (Bureiko *et al.* 2015) as well as aqueous film-forming foams for firefighting (Moody & Field 2000; Kovalchuk & Simmons 2021); and dispersion, preventing particle agglomeration in suspensions (Vaisman *et al.* 2006; Lotya *et al.* 2010). Moreover, the influence of surfactant on the hydrodynamics of drops is a fundamental scientific problem in its own right. Many experimental, theoretical, and computational studies have sought to elucidate the impact of surfactants on drop deformation, breakup, and motion, amongst other phenomena. In a number of cases, a quantitative understanding of the effects of surfactant is particularly desirable because these effects often contribute to discrepancies between theoretical predictions and observations in experiments, where drop systems are rarely truly clean. A classic example is that of a small drop sedimenting in an unbounded fluid, which has been repeatedly shown to obey Stokes' law for translating spheres rather than the Hadamard–Rybczynski equation (Savic 1953; Griffith 1962). This is explained by the presence of small amounts of surfactant that are convected to the trailing tip of the sedimenting drop, where they give rise to a stagnant cap, a region of the interface which is immobilised by the dense packing of surfactant molecules. The gradient in surfactant coverage leads to a gradient in surface tension, in turn leading to Marangoni stresses that suppress the surface flow and thereby decrease the terminal velocity of the drop (Levich 1962; Davis & Acrivos 1966; Sadhal & Johnson 1983).

Surfactants also play an important role in drop deformation and affect fluid flows both inside and outside the drop. A framework for calculating the shape and flow fields of an almost spherical drop in an arbitrary flow field accounting for surfactant was presented by Haber & Hetsroni (1972). Greenspan (1977) calculated the small deformations of a drop in an initially quiescent fluid with a prescribed deposition of surfactant to the interface. Flumerfelt (1980) developed a small-deformation theory for drops in shear or extensional flows that accounts for varying surface tension as well as surface viscosities, which resolved longstanding discrepancies between theoretical predictions (Taylor 1932, 1934; Cox 1969; Chaffey & Brenner 1967; Barthès-Biesel & Acrivos 1973) and experimental observations (Nawab & Mason 1958; Bartok & Mason 1959; Rumscheidt & Mason 1961) regarding the fluid circulation inside drops in shear flows. Sadhal & Johnson (1986) calculated the deformation of a sedimenting drop with an arbitrary prescribed surfactant distribution, and in the case of a stagnant cap distribution found that the drop deforms into a prolate spheroid. Stone & Leal (1990) studied the deformation and breakup of a surfactant-laden drop in an extensional flow using a boundary integral method accompanied by a small-deformation theory. This work was later generalised by Milliken *et al.* (1993) to capture transient breakup dynamics and to treat drop-fluid systems with nonidentical viscosities as well as interactions between surfactant molecules. The results of these studies highlighted two competing effects of variable surface tension, the balance of which determines the ultimate effect of the surfactant on the deformation. The first of these, known as tip stretching, occurs when surfactant is convected by the fluid flow away from the equator and towards the tips of the drop. Thus, the surface tension is decreased at the tips, where the interface must assume a greater degree of curvature to balance the normal stresses, leading to increased deformation when compared to a drop with uniform surface tension. This effect is particularly relevant when surfactant convection is strong relative to diffusion (large surface Péclet number). The second

effect, known as surface dilution, occurs due to the increasing surface area of the drop that accompanies deformation. The surfactant concentration is globally diluted, leading to a global increase in the surface tension and hence reduced deformation when compared to a drop with uniform surface tension, and often a higher critical strain rate for breakup. This effect is particularly relevant when diffusion is strong relative to convection (small surface Péclet number) or when the surface tension is highly sensitive to gradients in the surfactant concentration (in which case the resulting strong Marangoni stresses oppose the convective flux). The work of Stone & Leal (1990) assumes that the surfactant is insoluble in the bulk fluids and is present in dilute quantities only on the interface. In addition, surfactant solubility (Milliken & Leal 1994) and nondilute interfacial concentrations (Pawar & Stebe 1996; Eggleton & Stebe 1998; Eggleton *et al.* 1999) have also been investigated. Vlahovska *et al.* (2005) extended the theory of Stone & Leal (1990) to third order in the deformation. Other related studies include those on compound droplets (Mandal *et al.* 2016b) and the influence of Marangoni stresses on the rheology of emulsions of surfactant-laden drops in linear flows (Mandal *et al.* 2017).

Drop dynamics can also be controlled externally by applying an electric field. Depending on the electrical and mechanical properties of the fluids, such fields can induce a wide range of behaviours. To name a few, drop deformation (Taylor 1966; Ajayi 1978), breakup (Taylor 1964; Torza *et al.* 1971; Sherwood 1988) or coalescence (Allan & Mason 1961; Eow & Ghadiri 2003a; Ristenpart *et al.* 2009) can be either promoted or inhibited, translational motion can be induced (Baygents & Saville 1991; Eow & Ghadiri 2003b; Bandopadhyay *et al.* 2016), and emulsions of drops can exhibit various non-Newtonian behaviours, including significant changes to the apparent viscosity of the emulsion (Pan & McKinley 1997; Vlahovska 2011). A particularly extensive body of literature exists for the case of an uncharged, weakly conducting (leaky dielectric) drop immersed in another fluid. Early theories by O'Konski & Thacher (1953) and Allan & Mason (1962) assumed both fluids to be perfectly insulating and predicted that an initially spherical drop would elongate into a prolate spheroid along the field direction, owing to a balance between the electric stress normal to the interface and surface tension. Taylor (1966) proposed a leaky dielectric model (LDM) assuming that both fluids are electrically neutral and that free charge resides only at the drop surface. The surface charge density then satisfies a transport equation balancing a transient charging term, the Ohmic current between the bulk fluids, and charge convection by the interfacial velocity. The resulting charge distribution leads to an electric stress that has a component tangential to the drop surface, which cannot be balanced by uniform surface tension and therefore drives circulatory flows inside and outside the drop. At leading order in the drop deformation, the drop assumes an axisymmetric spheroidal shape that may be either prolate or oblate, depending on the ratios of the conductivities, permittivities, and viscosities of the two media. The induced fluid flow is also axisymmetric, and at the drop surface may be directed either from the poles of the drop to the equator or from the equator to the poles, depending on the ratios of the electrical properties of the fluids. This distinction leads to the common classification of leaky dielectric drops as one of prolate A (flow from the equator to the poles), prolate B (flow from the poles to the equator), and oblate (in which case the flow is always from the poles to the equator) (Lac & Homsy 2007).

The theoretical predictions of Taylor (1966) were accurate to first order in the electric capillary number (which measures the relative strengths of electric and capillary stresses) and thus valid only for small deviations of the drop from spherical shape. They underestimated the deformations observed in the experiments of Torza *et al.* (1971). Ajayi (1978) extended the small-deformation theory to second order in electric capillary number, but this refinement did not explain the discrepancy. Shortly thereafter, Vizika & Saville (1992) conducted new experiments that showed substantially better agreement with the theory of Taylor (1966)

than did the earlier measurements of Torza *et al.* (1971). Some residual discrepancies persisted for certain material systems, which the authors attributed to possible electric-field inhomogeneities or to surface charge conduction or convection neglected in the theoretical models. Out of these effects, charge convection has been shown to improve predictions of drop deformation. However, it is difficult to include in asymptotic models because it is inherently nonlinear. Hence, many existing works which retain charge convection use computational techniques including finite element (Feng 1999; Supeene *et al.* 2008), Volume-of-Fluid (López-Herrera *et al.* 2011; Dong & Sau 2023), boundary element (Lanauze *et al.* 2015; Das & Saintillan 2017a), and Lattice Boltzmann methods (Basu *et al.* 2024). These studies found that charge convection generally increases deformation for prolate drops and decreases deformation for oblate drops. The first of these is explained by the fact that prolate deformation is primarily due to the normal electric stresses on the surface, while viscous stresses associated with the electrohydrodynamic flow are less significant. Charge convection from the drop equator to the poles tends to strengthen the dipole moment of the interfacial charge distribution, leading to an increase in the deformation. Oblate deformation, on the other hand, may be dominated by either viscous or electric stresses. Charge convection in this case weakens both the dipole moment and the pole-to-equator electrohydrodynamic flow, leading to less deformation (Feng 1999). In strong electric fields, several authors have noted the formation of steep charge gradients (shocks) at the drop equator due to charge convection (Lanauze *et al.* 2015; Das & Saintillan 2017a; Firouznia *et al.* 2023; Peng *et al.* 2024; Peng & Schnitzer 2025).

Charge convection must also be included in three-dimensional models in order to capture a symmetry breaking instability known as Quincke rotation. This instability was first observed in solid spherical particles by Weiler (1893) and Quincke (1896) and leads to the spontaneous rotation of the sphere around an axis perpendicular to the applied field direction (Turcu 1987). It was first recognised by Lampa (1906) that in order for rotation to occur, the charge relaxation time of the sphere  $\tau_c^-$  ( $\tau_c^- = \epsilon^-/\sigma^-$ , where  $\epsilon$  is the absolute permittivity and  $\sigma$  is the conductivity of the sphere) must be longer than that of the surrounding fluid  $\tau_c^+$  ( $\tau_c^+ = \epsilon^+/\sigma^+$ , where  $\epsilon$  is the absolute permittivity and  $\sigma$  is the conductivity of the fluid). In this case, the surface charge distribution of the sphere is antiparallel to the applied field and the sphere is unstable. If an infinitesimal perturbation perpendicular to the electric field is applied to the sphere, a destabilising electric torque gives rise to steady rotation of the sphere when the electric field strength exceeds a critical value (Jones 1984). If the charge relaxation time of the sphere is shorter than that of the surrounding fluid, the dipole moment is parallel to the applied field, and any infinitesimal perturbation leads to an electric torque that returns the sphere to its stable equilibrium. Quincke rotation of solid particles has attracted attention particularly in studies of synthetic active matter (Bricard *et al.* 2013, 2015; Das & Lauga 2019; Han *et al.* 2021; Zhang *et al.* 2021b; Mauleon-Amieva *et al.* 2023; Reyes Garza *et al.* 2023; Fitzgerald *et al.* 2025). Recently, Quincke rotation of liquids has been exploited to generate a diverse range of non-equilibrium patterns, from rolling filaments and fluidic lattices to active emulsions under electrohydrodynamic confinement (Raju *et al.* 2021).

A theoretical treatment of Quincke rotation of drops is more challenging than that of solid spheres because of the deforming interface and the associated straining flow. Some theoretical models retain charge convection but are restricted to axisymmetric drops, and so are unable to capture Quincke rotation (Shutov 2002; Shkadov & Shutov 2002; Das & Saintillan 2017b). The first effort to capture Quincke rotation in a theoretical model was made by Feng (2002), who developed a 2D model valid for small values of the electric Reynolds number, which is the ratio of the conductive and convective time scales for charge redistribution. He *et al.* (2013) developed a small-deformation theory capable of capturing the transition to Quincke rotation, only including the rotational component of the flow in

the charge convection. Das & Saintillan (2021) extended that theory to include the straining flow in the charge convection. Experiments by Salipante & Vlahovska (2010, 2013) have also revealed the existence of hysteresis in the onset of Quincke rotation in drops, which has been reproduced in recent mathematical models (Peng & Schnitzer 2025; McDougall *et al.* 2025), and chaotic dynamics at higher field strengths.

The combined effect of surfactant and an electric field on drop dynamics has only been examined to a limited extent and is the focus of this paper. The first such study was Ha & Yang (1995), who developed a small-deformation theory accurate to second order in  $Ca_E$  with accompanying experiments. They found that surfactant enhances the deformation of both prolate and oblate drops, with a stronger effect for oblate drops owing to weaker surface convection in the prolate case. Teigen & Munkejord (2010) later used a level-set method to study surfactant effects across the three classes identified by Lac & Homsy (2007). Their results clarified that surfactant increases the deformation of prolate A and oblate drops but decreases that of prolate B drops, because surfactant is convected away from the poles and towards the equator. Nganguia *et al.* (2013) investigated nondiffusing surfactant using both a second-order small-deformation theory and a spheroidal model. As the surfactant concentration is varied, competing tip-stretching and surface-dilution effects produces a non-monotonic dependence of deformation on concentration. In subsequent work, Nganguia *et al.* (2019) incorporated surface diffusion and showed that increasing surfactant concentration strengthens (weakens) the deformation of prolate A drops and weakens (strengthens) that of prolate B drops when surface convection dominates (when diffusion dominates). Recent related studies include the boundary-integral simulations of Sorgentone *et al.* (2019) on electrohydrodynamic interactions between surfactant-laden drops, those of Han *et al.* (2022) incorporating dilational viscosity, and the hybrid lattice-Boltzmann/finite-difference simulations of Zhang *et al.* (2021a) on drops subjected to the combined effects of a shear flow and an electric field. To the best of our knowledge, the only studies to have considered the effects of surfactant while retaining charge convection are those of Poddar *et al.* (2018, 2019a,b), who have considered sedimenting drops and drops confined in Poiseuille flows. However, the effects of surfactant on Quincke rotation of drops have not yet been explored. Hence, in this work we develop a three-dimensional semi-analytical small-deformation theory that retains charge convection and is therefore able to capture the transition to Quincke rotation.

The article is organised as follows. In §2, we present the relevant governing equations and boundary conditions of the problem to be solved and summarise the nondimensionalisation and scaling assumptions. In §3 we present our solution to the problem. In §4, we discuss results of our theory, first for a drop in the Taylor regime and then for a drop in the Quincke regime. Finally, in §5, we outline the main results of the theory and indicate some avenues for future research.

## 2. Problem formulation

We consider an uncharged, neutrally buoyant leaky dielectric drop, immersed in an immiscible leaky dielectric fluid (Figure 1). The drop is coated with a dilute monolayer of insoluble, apolar surfactant. The electric permittivities of the fluids are denoted by  $\epsilon^\pm$ , the conductivities by  $\sigma^\pm$ , and the viscosities by  $\mu^\pm$ , where the plus subscript refers to the properties of the surrounding fluid, and the minus subscript refers to the properties of the drop. The drop domain is denoted by  $V^-$ , the surrounding fluid domain is denoted by  $V^+$ , and the interface between them is denoted by  $\partial V$ . The drop is initially spherical with radius  $a$ , but deforms upon the application of a uniform DC electric field  $\mathbf{E}_0$  pointing in the  $z$  direction. Upon the application of the field, free charge from both fluids accumulates at the

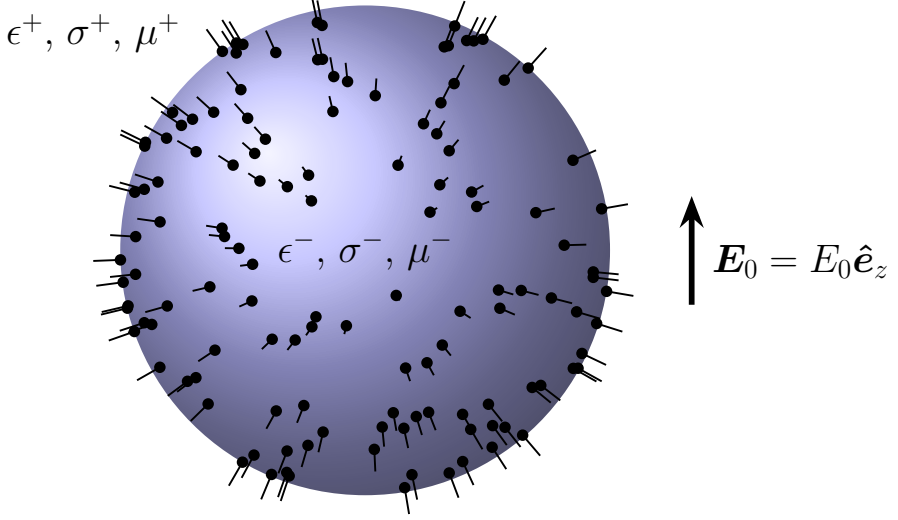


Figure 1: An uncharged, neutrally buoyant, leaky dielectric drop coated with a dilute monolayer of insoluble, apolar surfactant immersed in an immiscible leaky dielectric fluid. A uniform DC electric field is applied in the  $z$  direction,  $\mathbf{E}_0 = E_0 \hat{\mathbf{e}}_z$ .

drop interface, developing an interfacial charge distribution. Assuming that both of the fluids are electrically neutral, the electric field in each fluid domain,  $\mathbf{E}^\pm(\mathbf{r}, t)$ , is divergence free. Further, in the electrostatic limit, the electric field is irrotational, allowing the introduction of an electric potential  $\varphi^\pm(\mathbf{r}, t)$ , such that  $\mathbf{E}^\pm = -\nabla\varphi^\pm$ . The electric potential is governed by Laplace's equation in both the drop and the surrounding fluid,

$$\nabla^2 \varphi^\pm(\mathbf{r}, t) = 0 \quad \text{for } \mathbf{r} \in V^\pm. \quad (2.1)$$

The electric potential is continuous over the interface, and consequently so is the tangential component of the electric field,

$$[\![\varphi]\!] = 0, \quad [\![\mathbf{E} \cdot (\mathbf{I} - \mathbf{n}\mathbf{n})]\!] = \mathbf{0} \quad \text{for } \mathbf{r} \in \partial V, \quad (2.2)$$

where  $\mathbf{I}$  is the identity tensor,  $\mathbf{n}$  is a unit vector normal to the drop surface, pointing into the surrounding fluid, and the double bracket notation denotes the jump across the interface of any field variable defined in both the drop and surrounding fluid, i.e.  $[\![f]\!] = f^+(\mathbf{r}) - f^-(\mathbf{r})$  for  $\mathbf{r} \in \partial V$ . Conversely, the normal component of the electric field is discontinuous, and the interfacial charge density  $q$  is given by Gauss' law,

$$q = [\![\varepsilon \mathbf{E}]\!] \cdot \mathbf{n} \quad \text{for } \mathbf{r} \in \partial V. \quad (2.3)$$

Two mechanisms contribute to the evolution of  $q$ . The first is the Ohmic current jump across the interface, and the second is surface charge convection by the fluid flow. These are represented by the second and third terms, respectively, in the charge transport equation

$$\frac{\partial q}{\partial t} + [\![\sigma \mathbf{E} \cdot \mathbf{n}]\!] + \nabla_s \cdot (q \mathbf{v}) = 0 \quad \text{for } \mathbf{r} \in \partial V. \quad (2.4)$$

Here,  $(\mathbf{I} - \mathbf{n}\mathbf{n}) \cdot \nabla_s$  is the surface gradient operator. The presence of the fluid velocity  $\mathbf{v}(\mathbf{r}, t)$  renders (2.4) nonlinear, which makes analytical progress difficult. However, it is still amenable to numerical solution. In most of the relevant experiments and industrial applications, the drops are typically small (on the order of millimetres) and the fluids are rather viscous, so

we assume the Reynolds number of the flow to be small and hence inertia is neglected. The fluid velocity  $\mathbf{v}^\pm$  and dynamic pressure  $p^\pm$  then satisfy the Stokes equations in both domains,

$$\mu^\pm \nabla^2 \mathbf{v}^\pm = \nabla p^\pm, \quad \nabla \cdot \mathbf{v}^\pm = 0 \quad \text{for } \mathbf{r} \in V^\pm, \quad (2.5)$$

and the velocity is continuous across the interface,

$$[\![\mathbf{v}]\!] = \mathbf{0} \quad \text{for } \mathbf{r} \in \partial V. \quad (2.6)$$

The interface is advected with the flow, so the kinematic boundary condition, evaluated on the perturbed drop interface, can be expressed as

$$\frac{\partial f}{\partial t} = \mathbf{v} \cdot \mathbf{n} \quad \text{for } \mathbf{r} \in \partial V, \quad (2.7)$$

where  $f(\mathbf{r}, t)$  is a shape function to be defined in §3.1. The discontinuity of the material parameters between the drop and surrounding fluid gives rise to electric stresses on the interface, which are balanced by hydrodynamic, capillary and Marangoni stresses. This is expressed through a dynamic boundary condition given by

$$[\![f^E]\!] + [\![f^H]\!] = \gamma(\nabla_s \cdot \mathbf{n}) \mathbf{n} - \nabla_s \gamma \quad \text{for } \mathbf{r} \in \partial V, \quad (2.8)$$

where  $\nabla_s \cdot \mathbf{n} = 2\kappa_m$  is twice the mean surface curvature,  $\gamma = \gamma(\mathbf{r}, t)$  is the surface tension and  $[\![f^E]\!] = [\![\boldsymbol{\tau}^E]\!] \cdot \mathbf{n}$  and  $[\![f^H]\!] = [\![\boldsymbol{\tau}^H]\!] \cdot \mathbf{n}$  are the electric and hydrodynamic traction jumps across the interface, where

$$\boldsymbol{\tau}^E = \varepsilon \left( \mathbf{E} \mathbf{E} - \frac{1}{2} E^2 \mathbf{I} \right) \quad (2.9)$$

and

$$\boldsymbol{\tau}^H = -p \mathbf{I} + \mu \left( \nabla \mathbf{v} + \nabla \mathbf{v}^T \right) \quad (2.10)$$

are the electric and hydrodynamic stress tensors, respectively.

We assume the surface tension varies around the drop depending on the local surfactant distribution  $\Gamma$ , giving rise to tangential Marangoni stresses in the dynamic boundary condition, represented by the second term on the right hand side of (2.8). Gradients in  $\Gamma$  arise from convection by the fluid flow and are counteracted by surface diffusion. The evolution of  $\Gamma$  is therefore governed by the surface convection–diffusion equation,

$$\frac{\partial \Gamma}{\partial t} + \nabla_s \cdot (\mathbf{v}_s \Gamma) + (\nabla_s \cdot \mathbf{n})(\mathbf{v} \cdot \mathbf{n})\Gamma - D_s \nabla_s^2 \Gamma = 0 \quad \text{for } \mathbf{r} \in \partial V, \quad (2.11)$$

where  $D_s$  is the surface diffusivity of the surfactant (Stone 1990). The second and third terms correspond to surfactant convection. The precise relationship between the surface tension  $\gamma$  and the surfactant distribution  $\Gamma$  is not straightforward, and several equations of state have been proposed to capture various physical effects relevant in different regimes (Rosen & Kunjappu 2012; Manikantan & Squires 2020). Most commonly used is the Langmuir equation,

$$\gamma = \gamma_0 + RT \Gamma_\infty \ln \left( 1 - \frac{\Gamma}{\Gamma_\infty} \right), \quad (2.12)$$

where  $R$  is the gas constant,  $T$  is the absolute temperature,  $\Gamma_\infty$  is the maximum (i.e. the fully saturated) surfactant concentration and  $\gamma_0$  is the surface tension of the drop in the absence of surfactant. The Langmuir equation is generally valid for a wide range of surfactant concentrations, including those approaching  $\Gamma_\infty$ . However, for dilute concentrations of surfactant like those considered in this work, it is appropriate to linearise it about  $\Gamma = 0$ , in

which case the surface tension is given by

$$\gamma = \gamma_0 - RT\Gamma. \quad (2.13)$$

In the absence of external forcing, or in the limit of rapid diffusion, the surfactant distribution is uniform around the drop and is given by the equilibrium concentration  $\Gamma_{\text{eq}}$ . The corresponding surface tension at  $\Gamma = \Gamma_{\text{eq}}$  is  $\gamma = \gamma_{\text{eq}} (< \gamma_0)$ .

### 2.1. Nondimensionalisation and scaling assumptions

Permittivities, conductivities, and viscosities are scaled with  $\sigma^-$ ,  $\varepsilon^+$ , and  $\mu^+$ , which leads to three dimensionless numbers,

$$S = \frac{\sigma^+}{\sigma^-}, \quad Q = \frac{\varepsilon^-}{\varepsilon^+}, \quad \lambda = \frac{\mu^-}{\mu^+}. \quad (2.14)$$

We take the initial drop radius  $a$  as the characteristic length, the electrohydrodynamic flow time

$$\tau_{\text{EHD}} = \frac{\mu^+}{\varepsilon^+ E_0^2} \quad (2.15)$$

as the characteristic time, and  $\Gamma_{\text{eq}}$  and  $\gamma_{\text{eq}}$  as the characteristic surfactant concentration and surface tension, respectively. Other choices for the time scale which are sometimes used in studies of drop electrohydrodynamics include the Maxwell–Wagner relaxation time  $\tau_{\text{MW}} = (\varepsilon^- + 2\varepsilon^+)/(\sigma^- + 2\sigma^+)$ , which characterizes the timescale of dipole moment polarization and the angular velocity associated with Quincke rotation (Das & Saintillan 2017a,b, 2021), the charge relaxation time of the outer fluid  $\tau_c^+$  (Lanauze *et al.* 2015; Peng & Schnitzer 2025), and the capillary relaxation time  $\tau_\gamma = \mu^+ a / \gamma_0$ , which is the timescale for the drop to return to a spherical shape (Esmaeeli & Sharifi 2011; Esmaeeli & Behjatian 2020). The stress balance (2.8) can be written in nondimensional form as

$$[\![f^E]\!] + [\![f^H]\!] = \frac{1}{\text{Ca}_E} [\gamma(\nabla_s \cdot \mathbf{n})\mathbf{n} - \nabla_s \gamma] \quad \text{for } \mathbf{r} \in \partial V, \quad (2.16)$$

which includes the fourth dimensionless number, the electric capillary number  $\text{Ca}_E$ , defined as

$$\text{Ca}_E = \frac{\varepsilon^+ E_0^2 a}{\gamma_{\text{eq}}}. \quad (2.17)$$

It represents the ratio of electric to capillary stresses. We assume that the deviation of the drop shape from sphericity is small, in which case it is appropriate to follow the classical domain perturbation approach in which the flow fields are calculated assuming that the drop remains perfectly spherical (Taylor 1934; Cox 1969; Barthès-Biesel & Acrivos 1973). These flow fields are then used in the normal stress balance at the drop interface to determine the drop shape to first order in  $\delta$ , a small parameter quantifying the deviation of the drop shape from sphericity. It will be shown in §3.5 that  $\delta \propto \text{Ca}_E$ , hence we require  $\text{Ca}_E \ll 1$  in order for the drop to remain nearly spherical. If desired, the  $\mathcal{O}(\delta)$  drop shape can be used to obtain the corrections to the flow fields at the next order in  $\delta$ , but in the present work we describe only the leading order solution. Note that the uniform reduction of surface tension from that of the clean drop  $\gamma_0$  to that of the uniformly coated drop  $\gamma_{\text{eq}}$  is implicitly accounted for by using  $\gamma_{\text{eq}}$  to define  $\text{Ca}_E$ . Defining the capillary number this way allows us to focus on the effects of Marangoni stresses and spatial variations in the surface tension. The charge conservation equation (2.4) in nondimensional form is written

$$\frac{\partial q}{\partial t} + \frac{1}{\text{Re}_E} [\![\mathbf{j} \cdot \mathbf{n}]\!] + \nabla_s \cdot (qv) = 0 \quad \text{for } \mathbf{r} \in \partial V, \quad (2.18)$$

where

$$\text{Re}_E = \frac{\epsilon^{+2} E_0^2}{\sigma^+ \mu^+} \quad (2.19)$$

is the electric Reynolds number, which quantifies the rates of charge convection and relaxation relative to the rate of charging of the interface by Ohmic currents from the bulk fluids. In addition, the discontinuity of the normal current across the interface is given in nondimensional form by

$$[\![\mathbf{j} \cdot \mathbf{n}]\!] = \mathbf{E}^+ \cdot \mathbf{n} - \frac{1}{S} \mathbf{E}^- \cdot \mathbf{n}, \quad (2.20)$$

while the charge distribution  $q$  introduced in (2.3) is

$$q = (1 - Q) \hat{\mathbf{E}}_0 \cdot \hat{\mathbf{r}} + (2 + Q) \mathbf{P} \cdot \hat{\mathbf{r}}. \quad (2.21)$$

The surfactant transport equation (2.11) in nondimensional form is written

$$\frac{\partial \Gamma}{\partial t} + \nabla_s \cdot (\mathbf{v}_s \Gamma) + (\nabla_s \cdot \mathbf{n})(\mathbf{v} \cdot \mathbf{n})\Gamma - \frac{1}{\text{Pe}_s} \nabla_s^2 \Gamma = 0 \quad \text{for } \mathbf{r} \in \partial V, \quad (2.22)$$

where

$$\text{Pe}_s = \frac{\epsilon^+ E_0^2 a^2}{D_s \mu^+} \quad (2.23)$$

is the surface Péclet number, which is the ratio of the advective and diffusive surfactant transport rates. However, instead of treating  $\text{Pe}_s$  as an independent parameter, we instead define

$$\zeta = \frac{\text{Pe}_s}{\text{Re}_E}, \quad (2.24)$$

which is analogous to the parameter  $\gamma$  used in studies of drops in extensional flows (Stone & Leal 1990; Milliken *et al.* 1993), and is convenient because it characterises the strength of the diffusion of the surfactant while remaining independent of the electric field strength. Finally, the equation of state (2.13) in nondimensional form is written as

$$\gamma = 1 + \text{El} (1 - \Gamma). \quad (2.25)$$

Here,  $\text{El}$  denotes the elasticity number, defined as

$$\text{El} = \frac{RT\Gamma_{\text{eq}}}{\gamma_{\text{eq}}} = \frac{\gamma_0 - \gamma_{\text{eq}}}{\gamma_{\text{eq}}}, \quad (2.26)$$

which quantifies the variation of the surface tension as a function of the surfactant concentration. Changing  $\text{El}$  alters the sensitivity of the surface tension to variations in surfactant concentration, thereby modifying the strength of Marangoni stresses.

In general, the convective terms in both the charge transport and surfactant transport equations introduce nonlinearities that prevent closed-form analytical solutions. One possible approach is to linearize these equations and perform asymptotic expansions in  $\text{Re}_E$  and  $\text{Ca}_E$  simultaneously, but this can be cumbersome. Here we instead retain the nonlinear terms and solve the resulting equations numerically. The numerical solution of the charge transport equation is accurate in parameter regimes where charge convection by the induced straining flow remains weak, which occurs when  $\text{Re}_E = \mathcal{O}(1)$  and  $\lambda \gg 1$ . The solution of the surfactant transport remains accurate when the surfactant distribution remains almost uniform, which occurs either when  $\zeta \ll 1$  or when  $\text{Ca}_E/\text{El} \ll 1$ . In the present work, we adopt the latter assumption, and make no assumption about the magnitude of  $\zeta$ . Thus, given that  $\text{Ca}_E \ll 1$ , we therefore require  $\text{El} = \mathcal{O}(1)$ , consistent with Vlahovska *et al.* (2005).

### 3. Problem solution

We now describe the solution to the problem formulated in the previous section. In §3.1, we describe the definitions of the drop shape and surfactant distributions. In §3.2, we present the solution to Laplace's equation (2.1) based on a multipole expansion. In §3.3, we present the solution to the Stokes equations for the fluid velocity and pressure. In §3.4, we apply the kinematic boundary condition to relate the flow fields inside and outside the drop to one another and to the motion of the interface. In §3.5, we apply the stress boundary condition to relate the electric, hydrodynamic, capillary and Marangoni stresses at the interface. Finally, in §3.6 and §3.7, we use the charge and surfactant transport equations (2.18) and (3.7) to derive ordinary differential equations (ODEs) governing the evolutions of the dipole moment and surfactant distribution.

#### 3.1. Definitions of drop shape and surfactant distribution

In general, both the drop shape  $f(\theta, \phi, t)$  and the surfactant distribution  $\Gamma(\theta, \phi, t)$  can be expanded in a series of surface spherical harmonics. As mentioned previously, we assume the deviations of  $f$  and  $\Gamma$  from the spherical drop and the uniform surfactant distribution, respectively, are small. Then, in anticipation of the form of the electric stress and the resulting flow fields, we retain only the second-order harmonics, and so write

$$f(\theta, \phi, t) = 1 + \delta \mathbf{Q}^f : \hat{\mathbf{r}}\hat{\mathbf{r}}, \quad (3.1a)$$

$$\Gamma(\theta, \phi, t) = 1 + \epsilon \mathbf{Q}^\Gamma : \hat{\mathbf{r}}\hat{\mathbf{r}}. \quad (3.1b)$$

The double dot notation represents the scalar contraction of two tensors, and  $\hat{\mathbf{r}} = \mathbf{r}/r$  denotes the unit vector in the radial direction. Thus, for example,  $\mathbf{Q} : \hat{\mathbf{r}}\hat{\mathbf{r}} = Q_{ij}\hat{r}_i\hat{r}_j$ .  $\mathbf{Q}^f$  and  $\mathbf{Q}^\Gamma$  are symmetric irreducible second-order tensors each containing five independent coefficients. These coefficients are directly related to the five coefficients of a sum of  $\ell = 2$  associated Legendre polynomials and are referred to as the shape coefficients and the surfactant coefficients, respectively. In addition,  $\delta \ll 1$  and  $\epsilon \ll 1$  are small parameters which quantify the deviations of the drop shape from sphericity and the deviations of the surfactant distribution from the uniform coverage  $\Gamma_{\text{eq}}$ , respectively, both of which will be defined in §3.5.

Using the definition in (3.1a), the surface normal  $\mathbf{n}$  and the mean surface curvature  $\kappa_m$  of the interface are given by

$$\mathbf{n} = \frac{\hat{\mathbf{r}} - \nabla f}{|\hat{\mathbf{r}} - \nabla f|} = \hat{\mathbf{r}} - 2\delta(\mathbf{Q}^f \cdot \hat{\mathbf{r}}) \cdot (\mathbf{I} - \hat{\mathbf{r}}\hat{\mathbf{r}}), \quad \kappa_m = \frac{1}{2}\nabla_s \cdot \mathbf{n} = 1 + 2\delta\mathbf{Q}^f : \hat{\mathbf{r}}\hat{\mathbf{r}}. \quad (3.2)$$

#### 3.2. Electrostatics

To satisfy Laplace's equation (2.1), the electric potentials inside and outside the drop are expressed as multipole expansions. In the present work, only the dipole moment is retained. However, higher-order multipoles can be induced by charge convection by the induced straining flow. It will be shown in §3.5 that the leading-order straining flow, and hence the induced higher-order multipoles, appear at  $\mathcal{O}(\lambda^{-1})$ . However, the effect of these higher-order multipoles on the drop shape or flow fields appears only at  $\mathcal{O}(\lambda^{-2})$ . Hence, by retaining terms up to and including  $\mathcal{O}(\lambda^{-1})$ , the higher-order multipoles can be neglected and the potential inside and outside the drop can be written as

$$\varphi^- = \varphi_0 + \mathbf{P} \cdot \mathbf{r}, \quad \varphi^+ = \varphi_0 + r^{-3}\mathbf{P} \cdot \mathbf{r}, \quad (3.3)$$

respectively, where  $\varphi_0$  is the potential associated with the applied electric field and  $\mathbf{P}(t)$  denotes the induced dipole moment of the drop. The potentials inside and outside the drop

are given by growing and decaying harmonics, respectively. The electric fields inside and outside the drop are given by

$$\mathbf{E}^- = \hat{\mathbf{E}}_0 - \mathbf{P}, \quad \mathbf{E}_1 = \hat{\mathbf{E}}_0 - r^{-3} \mathbf{P} \cdot (\mathbf{I} - 3\hat{\mathbf{r}}\hat{\mathbf{r}}), \quad (3.4)$$

respectively. After calculating the electric stress tensor according to (2.9), the jump in electric traction across the drop interface can be written

$$[\![\mathbf{f}^E]\!] = [\![\boldsymbol{\tau}^E]\!] \cdot \hat{\mathbf{r}} = p^E \hat{\mathbf{r}} + \mathbf{Q}_{\hat{\mathbf{r}}}^E : \hat{\mathbf{r}}\hat{\mathbf{r}}\hat{\mathbf{r}} + \left( \mathbf{Q}_{\hat{\mathbf{r}}}^E \cdot \hat{\mathbf{r}} \right) \cdot (\mathbf{I} - \hat{\mathbf{r}}\hat{\mathbf{r}}) + \mathbf{T}^E \times \hat{\mathbf{r}}, \quad (3.5)$$

where

$$p^E = -\frac{1-Q}{6} + \frac{4-Q}{3} (\hat{\mathbf{E}}_0 \cdot \mathbf{P}) + \frac{Q+2}{6} P^2, \quad (3.6a)$$

$$\begin{aligned} \mathbf{Q}_{\hat{\mathbf{r}}}^E = & (1-Q)\hat{\mathbf{E}}_0\hat{\mathbf{E}}_0 + \frac{1+2Q}{2} (\hat{\mathbf{E}}_0\mathbf{P} + \mathbf{P}\hat{\mathbf{E}}_0) + \frac{5-2Q}{2} \mathbf{P}\mathbf{P} \\ & + \left[ -\frac{1-Q}{3} - \frac{1+2Q}{3} (\hat{\mathbf{E}}_0 \cdot \mathbf{P}) - \frac{5-2Q}{6} P^2 \right] \mathbf{I}, \end{aligned} \quad (3.6b)$$

$$\begin{aligned} \mathbf{Q}_{\hat{\mathbf{r}}}^E = & (1-Q)\hat{\mathbf{E}}_0\hat{\mathbf{E}}_0 + \frac{1+2Q}{2} (\hat{\mathbf{E}}_0\mathbf{P} + \mathbf{P}\hat{\mathbf{E}}_0) - (2+Q)\mathbf{P}\mathbf{P} \\ & + \left[ -\frac{1-Q}{3} - \frac{1+2Q}{3} (\hat{\mathbf{E}}_0 \cdot \mathbf{P}) + \frac{2+Q}{3} P^2 \right] \mathbf{I}, \end{aligned} \quad (3.6c)$$

$$\mathbf{T}^E = \frac{3}{2} \mathbf{P} \times \hat{\mathbf{E}}_0, \quad (3.6d)$$

where  $P = |\mathbf{P}|$ .

### 3.3. Hydrodynamics

We express the fluid velocity and pressure using the general solution of the Stokes equations (2.5) derived by Lamb (1932), given by

$$p = \sum_{n=-\infty}^{\infty} p_n, \quad (3.7a)$$

$$\mathbf{v} = \sum_{\substack{n=-\infty, \\ n \neq -1}}^{\infty} \left[ \boldsymbol{\nabla} \times (\mathbf{r}\chi_n) + \boldsymbol{\nabla}\phi_n + \frac{n+3}{2\mu(n+1)(2n+3)} r^2 \boldsymbol{\nabla} p_n - \frac{n}{\mu(n+1)(2n+3)} \mathbf{r} p_n \right]. \quad (3.7b)$$

Here,  $p_n$ ,  $\chi_n$  and  $\phi_n$  each denote a solid spherical harmonic of order  $n$  (Kim & Karrila 1991; Happel & Brenner 1983). Constant or growing harmonics (non-negative  $n$ ) can be expressed as the contraction of an irreducible symmetric tensor of order  $n$  and the tensor product of  $n$  unit position vectors,

$$p_n = r^n T_{i_1 i_2 i_3 \dots i_n}^{(n)} \hat{r}_{i_1} \hat{r}_{i_2} \hat{r}_{i_3} \dots \hat{r}_{i_n}, \quad (3.8)$$

with summation implied over  $i_1, i_2, i_3, \dots, i_n$ , and where  $T^{(n)}$  is an irreducible symmetric tensor. The decaying harmonics (negative  $n$ ) are similarly given by

$$p_{-n-1} = r^{-n-1} T_{i_1 i_2 i_3 \dots i_n}^{(n)} \hat{r}_{i_1} \hat{r}_{i_2} \hat{r}_{i_3} \dots \hat{r}_{i_n}, \quad (3.9)$$

with the  $\phi_n$  and  $\chi_n$  harmonics defined the same way. The general hydrodynamic stress on the drop surface associated with the velocity (3.7b) is

$$f^H = \mu \sum_{n=-\infty}^{\infty} \left[ (n-1) \nabla \times (\mathbf{r} \chi_n) + 2(n-1) \nabla \phi_n + \frac{n(n+2) \nabla p_n - (2n^2 + 4n + 3) \mathbf{r} p_n}{(n+1)(2n+3)} \right]. \quad (3.10)$$

We retain only growing harmonics in the solution inside the drop and decaying harmonics in the solution outside the drop, and then consider the resulting stresses on each side of the interface as given by (3.10). Then, by comparing the various stress modes with those in (3.5), we can deduce which harmonics need to be retained. After doing so, the velocities inside and outside the drop are

$$\mathbf{v}^- = \mathbf{d}^\chi \times \mathbf{r} + \mathbf{d}^\phi + 2\mathbf{q}^\phi \cdot \mathbf{r} + \frac{r^2 \mathbf{q}^P \cdot \mathbf{r}}{21\lambda} \cdot (5\mathbf{I} - 2\hat{\mathbf{r}}\hat{\mathbf{r}}), \quad (3.11)$$

$$\mathbf{v}^+ = r^{-3} \mathbf{D}^\chi \times \mathbf{r} + r^{-5} \frac{\mathbf{Q}^P : \mathbf{r} \mathbf{r} \mathbf{r}}{2} + r^{-5} (\mathbf{Q}^\phi \cdot \mathbf{r}) \cdot (2\mathbf{I} - 5\hat{\mathbf{r}}\hat{\mathbf{r}}), \quad (3.12)$$

respectively, where  $\mathbf{d}^\chi(t)$  and  $\mathbf{D}^\chi(t)$  are vectors corresponding to the solid body rotational flow induced by Quincke rotation,  $\mathbf{d}^\phi(t)$  is a uniform flow field inside the drop, and  $\mathbf{q}^P(t)$ ,  $\mathbf{Q}^P(t)$ ,  $\mathbf{q}^\phi(t)$ , and  $\mathbf{Q}^\phi(t)$  are second-order irreducible symmetric tensors corresponding to the straining flows induced by the quadrupolar electric stresses  $\mathbf{Q}_\ell^E$ . These vectors and tensors will henceforth be referred to as the flow coefficients. The hydrodynamic traction jump associated with (3.11) and (3.12) is

$$\begin{aligned} \llbracket f^H \rrbracket &= (\tilde{p}^- - \tilde{p}^+) \hat{\mathbf{r}} + \left( 24\mathbf{Q}^\phi - 3\mathbf{Q}^P - 4\lambda\mathbf{q}^\phi + \frac{\mathbf{q}^P}{7} \right) : \hat{\mathbf{r}}\hat{\mathbf{r}}\hat{\mathbf{r}} \\ &\quad + \left[ \left( -16\mathbf{Q}^\phi + \mathbf{Q}^P - \frac{16\mathbf{q}^P}{21} - 4\lambda\mathbf{q}^\phi \right) \cdot \hat{\mathbf{r}} \right] \cdot (\mathbf{I} - \hat{\mathbf{r}}\hat{\mathbf{r}}) - 3\mathbf{D}^\chi \times \hat{\mathbf{r}}, \end{aligned} \quad (3.13)$$

where  $\tilde{p}^-$  and  $\tilde{p}^+$  are the isotropic pressures inside and outside the drop, given by setting  $n = 0$  in (3.8) and (3.9), respectively.

### 3.4. Kinematic boundary condition

Next, we relate the flow coefficients in (3.11) and (3.12) to one another and to the motion of the interface using the tangential no-slip condition (2.6) along with the kinematic boundary condition (2.7). First, applying continuity of velocity tangential to the interface yields the relations

$$\mathbf{D}^\chi = \mathbf{d}^\chi, \quad \mathbf{0} = \mathbf{d}^\phi, \quad 2\mathbf{Q}^\phi = 2\mathbf{q}^\phi + \frac{5\mathbf{q}^P}{21\lambda}. \quad (3.14)$$

Second, expanding (2.7) yields

$$\mathbf{v}^- \cdot \hat{\mathbf{r}} - \delta \mathbf{v}^- \cdot \nabla (\mathbf{Q}^f : \hat{\mathbf{r}}\hat{\mathbf{r}}) = \mathbf{v}^+ \cdot \hat{\mathbf{r}} - \delta \mathbf{v}^+ \cdot \nabla (\mathbf{Q}^f : \hat{\mathbf{r}}\hat{\mathbf{r}}) = \delta \frac{\partial}{\partial t} (\mathbf{Q}^f : \hat{\mathbf{r}}\hat{\mathbf{r}}). \quad (3.15)$$

Since the solid body rotational flows  $\mathbf{D}^\chi$  and  $\mathbf{d}^\chi$  are independent of  $\lambda$  while the straining flow is assumed to be comparatively weak (scaling as  $\lambda^{-1}$ ), the velocities  $\mathbf{v}^\pm$  appearing in the nonlinear convective products  $\mathbf{v}^\pm \cdot \nabla f$  include only  $\mathbf{D}^\chi$  and  $\mathbf{d}^\chi$  at leading order. Given that  $\mathbf{d}^\chi = \mathbf{D}^\chi$ , then

$$\mathbf{v}^+ \cdot \nabla f = \mathbf{v}^- \cdot \nabla f = \left( \varepsilon_{ljk} Q_{li}^f D_k^\chi + \varepsilon_{lki} Q_{lj}^f D_k^\chi \right) \hat{r}_i \hat{r}_j = \mathbf{Q}^{\chi f} : \hat{\mathbf{r}}\hat{\mathbf{r}}, \quad (3.16)$$

where  $\varepsilon_{lkj}$  and  $\varepsilon_{lki}$  are the Levi–Civita tensor and

$$Q_{ij}^{\chi f} = \varepsilon_{lkj} Q_{li}^f D_k^{\chi} + \varepsilon_{lki} Q_{lj}^f D_k^{\chi}. \quad (3.17)$$

In the Taylor regime, this term has no effect since there is no rotational flow. In the Quincke regime, it acts to reduce the drop deformation by convecting away the shape distortions caused by the electric stresses and the straining flow. The kinematic condition can thus be written

$$\mathbf{v}^- \cdot \hat{\mathbf{r}} = \mathbf{v}^+ \cdot \hat{\mathbf{r}} = \delta \left( \frac{\partial \mathbf{Q}^f}{\partial t} + \mathbf{Q}^{\chi f} \right), \quad (3.18)$$

and substituting in the fluid velocities given in (3.11) and (3.12) yields

$$2\mathbf{q}^{\phi} + \frac{1}{7\lambda} \mathbf{q}^p = \frac{1}{2} \mathbf{Q}^p - 3\mathbf{Q}^{\phi} = \delta \left( \frac{\partial \mathbf{Q}^f}{\partial t} + \mathbf{Q}^{\chi f} \right). \quad (3.19)$$

Combining this with the relations given in (3.14) allows us to express the flow coefficients  $\mathbf{Q}^{\phi}$ ,  $\mathbf{q}^{\phi}$  and  $\mathbf{q}^p$  in terms of  $\mathbf{Q}^p$  and  $\delta(\partial \mathbf{Q}^f / \partial t + \mathbf{Q}^{\chi f})$ :

$$\mathbf{Q}^{\phi} = \frac{1}{6} \mathbf{Q}^p - \frac{\delta}{3} \left( \frac{\partial \mathbf{Q}^f}{\partial t} + \mathbf{Q}^{\chi f} \right), \quad (3.20a)$$

$$\mathbf{q}^p = \frac{7\lambda}{2} \mathbf{Q}^p - \frac{35\lambda\delta}{2} \left( \frac{\partial \mathbf{Q}^f}{\partial t} + \mathbf{Q}^{\chi f} \right), \quad (3.20b)$$

$$\mathbf{q}^{\phi} = -\frac{1}{4} \mathbf{Q}^p + \frac{7\delta}{4} \left( \frac{\partial \mathbf{Q}^f}{\partial t} + \mathbf{Q}^{\chi f} \right). \quad (3.20c)$$

The hydrodynamic traction (3.13) can be rewritten as

$$[\![f^H]\!] = [\![\boldsymbol{\tau}^H]\!] \cdot \hat{\mathbf{r}} = p^H \hat{\mathbf{r}} + \mathbf{Q}_{\hat{\mathbf{r}}}^H : \hat{\mathbf{r}} \hat{\mathbf{r}} \hat{\mathbf{r}} + \left( \mathbf{Q}_{\hat{\mathbf{r}}}^H \cdot \hat{\mathbf{r}} \right) \cdot (\mathbf{I} - \hat{\mathbf{r}} \hat{\mathbf{r}}) + \mathbf{T}^H \times \hat{\mathbf{r}}, \quad (3.21)$$

where

$$p^H = \tilde{p}^- - \tilde{p}^+, \quad (3.22a)$$

$$\mathbf{Q}_{\hat{\mathbf{r}}}^H = \frac{2+3\lambda}{2} \mathbf{Q}^p - \frac{16+19\lambda}{2} \delta \left( \frac{\partial \mathbf{Q}^f}{\partial t} + \mathbf{Q}^{\chi f} \right), \quad (3.22b)$$

$$\mathbf{Q}_{\hat{\mathbf{r}}}^H = -\frac{5(1+\lambda)}{3} \mathbf{Q}^p + \frac{16+19\lambda}{3} \delta \left( \frac{\partial \mathbf{Q}^f}{\partial t} + \mathbf{Q}^{\chi f} \right), \quad (3.22c)$$

$$\mathbf{T}^H = -3\mathbf{D}^{\chi}. \quad (3.22d)$$

### 3.5. Stress balance

We now apply the dynamic boundary condition (2.16), enforcing a balance between the electric and hydrodynamic stresses (3.5) and (3.21), the Marangoni stresses arising from nonuniform surface tension, and the usual capillary stresses. Expanding the right-hand side of (2.16) yields

$$[\![f^E]\!] + [\![f^H]\!] = \frac{2}{\text{Ca}_E} \hat{\mathbf{r}} - \frac{4}{\text{Ca}_E} \delta(\mathbf{Q}^f \cdot \mathbf{r}) \cdot (\mathbf{I} - 2\hat{\mathbf{r}}\hat{\mathbf{r}}) + \frac{2\text{El}}{\text{Ca}_E} \boldsymbol{\epsilon}(\mathbf{Q}^F \cdot \hat{\mathbf{r}}) \cdot (\mathbf{I} - 2\hat{\mathbf{r}}\hat{\mathbf{r}}). \quad (3.23)$$

Considering the radial component of (3.23), we obtain a balance of isotropic pressures and quadrupolar stresses, which yields two equations; one for the pressures,

$$p^H = -p^E + \frac{2}{\text{Ca}_E}, \quad (3.24)$$

and one for the quadrupolar stresses,

$$\mathbf{Q}_f^H = \frac{2}{Ca_E} \left( -El\epsilon\mathbf{Q}^\Gamma + 2\delta\mathbf{Q}^f \right) - \mathbf{Q}_f^E. \quad (3.25)$$

In order for the capillary stresses to balance the  $O(1)$  electric and hydrodynamic stresses, we require  $\delta \propto Ca_E$ , and following previous work (Taylor 1966) we choose

$$\delta = \frac{3Ca_E}{4(1+2S)^2}. \quad (3.26)$$

Analogously, for the Marangoni stresses to balance the electrostatic and hydrodynamic stresses, we require  $\epsilon \propto Ca_E/El$ , and so define

$$\epsilon = \frac{Ca_E}{El}, \quad (3.27)$$

which is the reciprocal of the usual Marangoni number.

Next, examining the tangential components of (3.23) we have a balance of quadrupolar stresses and torques, which again yields two equations; one for the quadrupolar stresses,

$$\mathbf{Q}_i^H = \frac{2El}{Ca_E} \epsilon \mathbf{Q}^\Gamma - \mathbf{Q}_i^E, \quad (3.28)$$

and one for the torques,

$$\mathbf{T}^H = -\mathbf{T}^E. \quad (3.29)$$

Substituting the expressions for the quadrupolar hydrodynamic stresses (3.22b) and (3.22c) into (3.25) and (3.28) gives two equations for the flow coefficients  $\mathbf{Q}^P$  and the shape evolution  $\partial\mathbf{Q}^f/\partial t$ , which are then given by

$$\mathbf{Q}^P = \frac{2}{3+2\lambda} \left[ -\frac{3}{(1+2S)^2} \mathbf{Q}^f + \mathbf{Q}_f^E + \frac{3}{2} \mathbf{Q}_i^E - \frac{El}{Ca_E} \epsilon \mathbf{Q}^\Gamma \right] \quad (3.30)$$

and

$$\begin{aligned} \frac{\partial \mathbf{Q}^f}{\partial t} = & \frac{10(1+\lambda)}{\delta(16+19\lambda)(3+2\lambda)} \left[ -\frac{3}{(1+2S)^2} \mathbf{Q}^f + \mathbf{Q}_f^E \right. \\ & \left. + \frac{6+9\lambda}{10(1+\lambda)} \mathbf{Q}_i^E + \frac{(4+\lambda)El}{5(1+\lambda)Ca_E} \epsilon \mathbf{Q}^\Gamma \right] - \mathbf{Q}^{\chi f}. \end{aligned} \quad (3.31)$$

Substituting the electric and hydrodynamic torques given in (3.6d) and (3.22d) into (3.29), we find

$$\mathbf{D}^\chi = \frac{1}{2} \mathbf{P} \times \hat{\mathbf{E}}_0. \quad (3.32)$$

At this point, the flow fields and drop shape are known in terms of the dipole moment  $\mathbf{P}$  and the surfactant coefficients in  $\mathbf{Q}^\Gamma$ , which will be determined in the following sections via application of their respective transport equations.

### 3.6. Charge transport

The dipole moment evolves according to the dimensionless charge transport equation (2.4) at the interface of the drop. Substituting the fluid velocity from either (3.11) or (3.12), the charge density (2.21) and the normal current jump (2.20) into (2.18) yields an evolution

equation for the dipole moment  $\mathbf{P}$ :

$$\begin{aligned} \frac{d\mathbf{P}}{dt} = & -\frac{1}{\text{Re}_E} \frac{1+2S}{S(2+Q)} \mathbf{P} - \frac{1}{\text{Re}_E} \frac{S-1}{S(2+Q)} \hat{\mathbf{E}}_0 + \mathbf{D}^\chi \times \left( \frac{1-Q}{2+Q} \hat{\mathbf{E}}_0 + \mathbf{P} \right) \\ & + \left( \frac{1-Q}{2+Q} \hat{\mathbf{E}}_0 + \mathbf{P} \right) \cdot \left( \frac{1}{5} \mathbf{Q}^p - \frac{6}{5} \delta \left( \frac{\partial \mathbf{Q}^f}{\partial t} + \mathbf{Q}^{\chi f} \right) \right). \end{aligned} \quad (3.33)$$

A solution for which  $\mathbf{P}$  is parallel or antiparallel to  $\hat{\mathbf{E}}_0$  always exists, in which case Quincke rotation is impossible, is evident from (3.32). However, above a critical field strength, a solution in which the dipole moment has a transverse component also exists, which leads to Quincke rotation. For a solid sphere, the critical field strength is given by

$$E_{c,s} = \sqrt{\frac{2\mu^+(2+Q)(1+2S)}{3\epsilon^+ \tau_{\text{MW}}(SQ-1)}}, \quad (3.34)$$

as first derived by Jones (1984).

### 3.7. Surfactant transport

The surfactant distribution evolves according to the dimensionless transport equation (2.22). Substituting in  $\Gamma$  from (3.1b),  $\mathbf{v}$  from (3.11) or (3.12),  $\mathbf{n}$  and  $\kappa_m$  from (3.2), and retaining leading-order terms, we obtain a system of ODEs for the quadrupole  $\mathbf{Q}^\Gamma$ ,

$$\frac{\partial \mathbf{Q}^\Gamma}{\partial t} = \frac{1}{\epsilon} \mathbf{Q}^p - 4 \frac{\delta}{\epsilon} \left( \frac{\partial \mathbf{Q}^f}{\partial t} + \mathbf{Q}^{\chi f} \right) - \mathbf{Q}^{\chi \Gamma} - \frac{6}{\zeta \text{Re}_E} \mathbf{Q}^\Gamma, \quad (3.35)$$

where

$$Q_{ij}^{\chi \Gamma} = Q_{il}^\Gamma \epsilon_{ljk} D_k^\chi + Q_{jl}^\Gamma \epsilon_{lki} D_k^\chi. \quad (3.36)$$

Analogously to  $\mathbf{Q}^{\chi f}$  as defined in (3.17),  $\mathbf{Q}^{\chi \Gamma}$  acts to restore a uniform surfactant distribution after Quincke rotation begins.

### 3.8. Summary of differential equations

The full system of nonlinear ODEs governing the system is written compactly as

$$\frac{d}{dt} \begin{bmatrix} \mathbf{P} \\ \mathbf{Q}^f \\ \mathbf{Q}^\Gamma \end{bmatrix} = \mathcal{F} \left( \mathbf{P}, \mathbf{Q}^f, \mathbf{Q}^\Gamma; \text{Ca}_E, \text{Re}_E, \zeta, \text{El}, \epsilon, Q, S, \lambda \right). \quad (3.37)$$

We use an explicit fourth-order Runge-Kutta method (RK4) to integrate the system of equations (3.37). However, this procedure only allows us to obtain stable steady state solutions, and so in order to obtain unstable steady state solutions, we use a pseudo-arc length continuation algorithm. For the RK4 method, the initial conditions are those of an initially spherical drop with uniform surfactant distribution,  $\mathbf{Q}^f(0) = \mathbf{Q}^\Gamma(0) = \mathbf{0}$ , and zero surface charge density  $q(\mathbf{r}, 0) = 0$ . The charge density condition when substituted into (2.21) gives the initial condition for the dipole moment,

$$\mathbf{P}(0) = \frac{Q-1}{2+Q} \hat{\mathbf{E}}_0. \quad (3.38)$$

For the pseudo-arc length continuation algorithm, we use the MATLAB nonlinear solver `fsolve` as a corrector at each iteration and initial solutions are calculated using equations for the base state variables that will be given in §4.1.

## 4. Results

In this section, we present results obtained from the model described in the previous sections. In §4.1, we describe the linearisation of the differential equations derived in the previous section, which is used to examine the stability of the system. In §4.2, we demonstrate that the predictions of the present model are in agreement with those of earlier models. In §4.3, we investigate the combined effects of surfactant and charge convection on the drop dynamics in the Taylor regime. In §4.4, we explore how surfactant effects impact the stability and angular velocity of a drop in the Quincke regime.

### 4.1. Linear stability analysis

To investigate the onset of Quincke rotation, we linearly perturb the system around a steady, axisymmetric base state corresponding to a drop in the Taylor regime which allows us to perform the analysis in the  $xz$  plane without loss of generality. Denoting base state quantities by a zero subscript, axisymmetry implies

$$P_{0,x} = Q_{0,xz}^\Gamma = Q_{0,xz}^f = 0, \quad Q_{0,xx}^\Gamma = Q_{0,yy}^\Gamma, \quad Q_{0,xx}^f = Q_{0,yy}^f. \quad (4.1)$$

Therefore,  $\mathbf{D}_0^\chi = \mathbf{0}$  and so  $\mathbf{Q}_0^{\chi f} = \mathbf{Q}_0^{\chi \Gamma} = \mathbf{0}$ . Explicitly, we perturb the variables as

$$\begin{pmatrix} P_x \\ P_z \\ Q_{xx}^f \\ Q_{zz}^f \\ Q_{xz}^f \\ Q_{xx}^\Gamma \\ Q_{zz}^\Gamma \\ Q_{xz}^\Gamma \end{pmatrix} = \begin{pmatrix} 0 \\ P_{0,z} \\ Q_{0,xx}^f \\ Q_{0,zz}^f \\ 0 \\ Q_{0,xx}^\Gamma \\ Q_{0,zz}^\Gamma \\ 0 \end{pmatrix} + \Delta \begin{pmatrix} P_{\Delta,x} \\ P_{\Delta,z} \\ Q_{\Delta,xx}^f \\ Q_{\Delta,zz}^f \\ Q_{\Delta,xz}^f \\ Q_{\Delta,xx}^\Gamma \\ Q_{\Delta,zz}^\Gamma \\ Q_{\Delta,xz}^\Gamma \end{pmatrix}, \quad (4.2)$$

where the small parameter  $\Delta \ll 1$  is a measure of the size of the perturbations to the variables, and the  $\Delta$  subscript denotes the perturbed variables. The  $z$  component of the base state dipole moment,  $P_{0,z}$ , is computed from a cubic equation derived from the charge transport equation (2.18), namely,

$$\mathcal{A}P_{0,z}^3 + \mathcal{B}P_{0,z}^2 + CP_{0,z} + \mathcal{D} = 0, \quad (4.3)$$

where

$$\mathcal{A} = -\frac{2(2+Q)}{25(1+\lambda) + 5\frac{\text{El}}{\text{Ca}_E}\epsilon}, \quad (4.4a)$$

$$\mathcal{B} = \frac{6Q}{25(1+\lambda) + 5\frac{\text{El}}{\text{Ca}_E}\epsilon}, \quad (4.4b)$$

$$C = -1 + \frac{6(1-Q^2)}{25(2+Q)(1+\lambda) + 5(2+Q)\frac{\text{El}}{\text{Ca}_E}\epsilon}, \quad (4.4c)$$

$$\mathcal{D} = \frac{1-S}{1+2S} + \frac{2(1-Q)^2}{25(2+Q)(1+\lambda) + 5(2+Q)\frac{\text{El}}{\text{Ca}_E}\epsilon}, \quad (4.4d)$$

which must be solved numerically. The base state surfactant coefficients are given by

$$Q_{0,xx}^{\Gamma} = -\frac{1-Q+(1+2Q)P_{0,z}-(2+Q)P_{0,z}^2}{\epsilon \left( 30(1+\lambda) \frac{1}{\zeta \text{Re}_E} + 6 \frac{\text{El}}{\text{Ca}_E} \right)}, \quad (4.5a)$$

$$Q_{0,zz}^{\Gamma} = -2Q_{0,xx}^{\Gamma}, \quad (4.5b)$$

and the base state shape coefficients are

$$Q_{0,xx}^f = \frac{(1+2S)^2}{3} \left[ -\frac{3}{2}P_{0,z}^2 - \frac{(16+19\lambda)\frac{1}{\zeta \text{Re}_E} + 4\frac{\text{El}}{\text{Ca}_E}}{30(1+\lambda)\frac{1}{\zeta \text{Re}_E} + 6\frac{\text{El}}{\text{Ca}_E}} \right. \\ \left. \times \left( 1-Q+(1+2Q)P_{0,z}-(2+Q)P_{0,z}^2 \right) \right], \quad (4.6a)$$

$$Q_{0,zz}^f = -2Q_{0,xx}^f. \quad (4.6b)$$

Ultimately, the resulting linear system can be written as

$$\frac{d}{dt} \begin{pmatrix} P_{\Delta,x} \\ P_{\Delta,z} \\ Q_{\Delta,xx}^f \\ Q_{\Delta,zz}^f \\ Q_{\Delta,xz}^f \\ Q_{\Delta,xz}^{\Gamma} \\ Q_{\Delta,xx}^{\Gamma} \\ Q_{\Delta,zz}^{\Gamma} \\ Q_{\Delta,xz}^{\Gamma} \end{pmatrix} = \begin{bmatrix} J_{11} & 0 & 0 & 0 & J_{15} & 0 & 0 & J_{18} \\ 0 & J_{22} & 0 & J_{24} & 0 & 0 & J_{27} & 0 \\ 0 & J_{32} & J_{33} & 0 & 0 & J_{36} & 0 & 0 \\ 0 & J_{42} & 0 & J_{44} & 0 & 0 & J_{47} & 0 \\ J_{51} & 0 & 0 & 0 & J_{55} & 0 & 0 & J_{58} \\ 0 & J_{62} & J_{63} & 0 & 0 & J_{66} & 0 & 0 \\ 0 & J_{72} & 0 & J_{74} & 0 & 0 & J_{77} & 0 \\ J_{81} & 0 & 0 & 0 & J_{85} & 0 & 0 & J_{88} \end{bmatrix} \begin{pmatrix} P_{\Delta,x} \\ P_{\Delta,z} \\ Q_{\Delta,xx}^f \\ Q_{\Delta,zz}^f \\ Q_{\Delta,xz}^f \\ Q_{\Delta,xz}^{\Gamma} \\ Q_{\Delta,xx}^{\Gamma} \\ Q_{\Delta,zz}^{\Gamma} \\ Q_{\Delta,xz}^{\Gamma} \end{pmatrix}, \quad (4.7)$$

where, for brevity, the elements of the Jacobian matrix are given in appendix A. The electric field strength is increased until one of the eigenvalues of the Jacobian has a positive real part, indicating instability.

#### 4.2. Validation

In this section, we demonstrate that the present model recovers the linear term of the second-order small-deformation theory of Nganguia *et al.* (2013) in the limits of zero electric Reynolds number,  $\text{Re}_E \rightarrow 0$ , and zero surfactant diffusion,  $\text{Pe}_s \rightarrow \infty$  or equivalently  $\zeta \rightarrow \infty$ . Our model also reduces to that of Stone & Leal (1990) if the electric field is switched off and the drop is instead exposed to an extensional flow.

First, we consider the behaviour of a drop in the Taylor regime in the limit of zero surfactant diffusion, as studied by Nganguia *et al.* (2013). In this limit, the flow is completely arrested once the surfactant has been redistributed such that the Marangoni stresses balance the electric stresses. Therefore, charge convection can have no impact on the steady drop shape or surfactant distribution, although it can have a transient impact while the surfactant is being redistributed. At steady state, in the absence of charge convection, the charge transport equation simplifies to

$$[\![ j \cdot \hat{r} ]\!] = 0, \quad (4.8)$$

which yields a simple expression for the dipole moment,

$$\mathbf{P} = \frac{1-S}{1+2S} \hat{\mathbf{E}}_0. \quad (4.9)$$

Hence, if charge convection is absent, then the dipole moment is either parallel or anti-parallel to the applied field and Quincke rotation is impossible, as is clear from (3.32). Then, the terms associated with rotation ( $\mathbf{Q}^{\chi f}$  and  $\mathbf{Q}^{\chi \Gamma}$ ) may be removed from the ODE for the surfactant quadrupole (3.35), which in the limit  $\zeta \rightarrow \infty$  becomes

$$\frac{\partial \mathbf{Q}^{\Gamma}}{\partial t} = \frac{1}{\epsilon} \mathbf{Q}^P + 4 \frac{\delta}{\epsilon} \frac{\partial \mathbf{Q}^f}{\partial t}. \quad (4.10)$$

Evidently, at steady state we have  $\mathbf{Q}^P = \mathbf{0}$ . Using this result together with (4.9) allows us to obtain algebraic solutions of Eqs. (3.30) and (3.31), yielding

$$\mathbf{Q}^f = \frac{3}{2} \left( 4S(1 - SQ) + (1 - S)^2 \right) \left( \hat{\mathbf{E}}_0 \hat{\mathbf{E}}_0 - \frac{1}{3} \mathbf{I} \right) \quad (4.11a)$$

and

$$\mathbf{Q}^{\Gamma} = \frac{9S(1 - SQ)}{2(1 + 2S)^2} \left( \hat{\mathbf{E}}_0 \hat{\mathbf{E}}_0 - \frac{1}{3} \mathbf{I} \right). \quad (4.11b)$$

Thus, the sign of the discriminating function  $4S(1 - SQ) + (1 - S)^2$  determines the prolate (positive) or oblate (negative) nature of the deformation, as found by Nganguia *et al.* (2013). To quantify the deformation, we use the parameter  $D_Q$ , defined as

$$D_Q = \frac{L - B}{L + B}, \quad (4.12)$$

where  $L$  and  $B$  are the long and short axes of the drop in the  $xz$  plane. In the Taylor regime, the drop adopts a steady spheroidal shape and  $L$  and  $B$  are parallel and perpendicular to the applied field, or vice versa. In the Quincke regime, the drop adopts a steady tilted shape with its longest axis misaligned with the  $z$  axis (in the case of a prolate  $B$  drop) or the  $x$  axis (in the case of an oblate drop) by an angle which we denote  $\theta_T$ . The deformation parameter  $D_Q$  can be written as

$$D_Q = \frac{1}{2} \delta |Q_{xx}^f - Q_{zz}^f| \sqrt{1 + \left( \frac{2Q_{xz}^f}{Q_{xx}^f - Q_{zz}^f} \right)^2} + O(\delta^2). \quad (4.13)$$

Note that  $D_Q$  is always positive, unlike the more commonly used deformation parameter  $D = (l_{\parallel} - l_{\perp})/(l_{\parallel} + l_{\perp})$ , where  $l_{\parallel}$  and  $l_{\perp}$  are the lengths of the axes of the drop parallel and perpendicular to the applied field, respectively. In the Taylor regime,  $Q_{xz}^f = 0$  so  $D_Q = \frac{1}{2} \delta |Q_{xx}^f - Q_{zz}^f|$ , in which case  $D_Q = |D|$ . Using this expression, the steady drop shape (4.11a) corresponds to a deformation of

$$D_Q = \frac{9\text{Ca}_E}{16(1 + 2S)^2} |4S(1 - SQ) + (1 - S)^2|, \quad (4.14)$$

which is equivalent to the linear term of Eq. (18) of Nganguia *et al.* (2013), up to the sign convention for oblate deformations.

Next, to demonstrate consistency with the results of the model of Stone & Leal (1990), we consider the case in which diffusion is strong, and replace the electric field with an imposed straining flow of the form

$$\mathbf{v}^{\infty} = \mathbf{S}_e \cdot \mathbf{r} = \pm k \begin{bmatrix} -\frac{1}{2} & 0 & 0 \\ 0 & -\frac{1}{2} & 0 \\ 0 & 0 & 1 \end{bmatrix} \cdot \mathbf{r}, \quad (4.15)$$

where  $k$  is the shear rate. Equation (4.15) corresponds to a uniaxial extensional flow for

positive  $k$ , and a biaxial extensional flow for negative  $k$ . These flow fields have been studied by Stone & Leal (1990) for low  $\text{Pe}_s$  and involve qualitatively similar convective fluxes at the drop surface to those induced by a prolate A drop (uniaxial extension) or an oblate or prolate B drop (biaxial extension) exposed an electric field. In either case, the surfactant transport equation (3.35) becomes

$$\frac{\partial \mathbf{Q}^\Gamma}{\partial t} = \frac{1}{\epsilon} \mathbf{Q}^P - 4 \frac{\text{Ca}}{\epsilon} \frac{\partial \mathbf{Q}^f}{\partial t} + \frac{5}{\epsilon} \mathbf{S}_e - \frac{6}{\text{Pe}_s} \mathbf{Q}^\Gamma, \quad (4.16)$$

where

$$\text{Ca} = \frac{\mu^+ k a}{\gamma_{\text{eq}}} \ll 1 \quad (4.17)$$

is the capillary number, which represents the ratio of viscous to capillary stresses. Also, the Péclet number for the extensional flow is

$$\text{Pe}_s = \frac{k a^2}{D_s}, \quad (4.18)$$

and the flow coefficients in  $\mathbf{Q}^P$  are given by

$$\mathbf{Q}^P = \frac{2}{3 + 2\lambda} \left( -4\mathbf{Q}^f - \frac{\text{El}}{\text{Ca}} \epsilon \mathbf{Q}^\Gamma + 5(1 - \lambda) \mathbf{S}_e \right). \quad (4.19)$$

In addition, the drop shape evolves according to

$$\frac{\partial \mathbf{Q}^f}{\partial t} = \frac{1}{\text{Ca}(3 + 2\lambda)} \left( -\frac{40(1 + \lambda)}{(16 + 19\lambda)} \mathbf{Q}^f + \frac{2(4 + \lambda)}{(16 + 19\lambda)} \frac{\text{El}}{\text{Ca}} \epsilon \mathbf{Q}^\Gamma + 5\mathbf{S}_e \right). \quad (4.20)$$

Then,  $\mathbf{Q}^\Gamma$  can be eliminated between (4.16) and (4.20) to form an equation for  $\partial \mathbf{Q}^\Gamma / \partial t$  in terms of  $\partial \mathbf{Q}^f / \partial t$ ,  $\mathbf{Q}^f$  and  $\mathbf{S}_e$ . Differentiating (4.20) and substituting in this equation gives a second order ODE for  $\mathbf{Q}^f$  which is decoupled from  $\mathbf{Q}^\Gamma$ ,

$$\begin{aligned} & \frac{(3 + 2\lambda)(16 + 19\lambda)}{2} \frac{\text{Ca}^2}{\text{El}} \frac{\partial^2 \mathbf{Q}^f}{\partial t^2} + \left[ (32 + 23\lambda)\text{Ca} + 20(1 + \lambda) \frac{\text{Ca}}{\text{El}} \right. \\ & \left. + 3(3 + 2\lambda)(16 + 19\lambda) \frac{\text{Ca}^2}{\text{ElPe}_s} \right] \frac{\partial \mathbf{Q}^f}{\partial t} + 24 \left[ 1 + 5(1 + \lambda) \frac{\text{Ca}}{\text{Pe}_s} \right] \mathbf{Q}^f \\ & = 15 \left[ 4 + (16 + 19\lambda) \frac{\text{Ca}}{\text{ElPe}_s} \right] \mathbf{S}_e, \end{aligned} \quad (4.21)$$

which is equivalent to Eq. (22) of Stone & Leal (1990). A similar decoupled ODE can be written for  $\mathbf{Q}^\Gamma$ .

### 4.3. Taylor regime

In this section, we study the combined effects of surfactant and charge convection on the drop dynamics in the Taylor regime.

#### 4.3.1. Transient behaviour

First, Figure 2(a) shows the evolution of the tangential electric (yellow lines), hydrodynamic (blue lines) and Marangoni (dark red lines) stresses on the surface of a prolate A drop for which  $S = 1/3$ ,  $Q = 1$ ,  $\lambda = 10$ . Specifically, we plot  $\sigma^E$ ,  $\sigma^H$  and  $\sigma^M$ , defined as

$$\sigma^E = Q_{\hat{\mathbf{t}},zz}^E, \quad \sigma^H = Q_{\hat{\mathbf{t}},zz}^H, \quad \sigma^M = -2 \frac{\text{El}\epsilon}{\text{Ca}_E} Q_{zz}^\Gamma. \quad (4.22a)$$

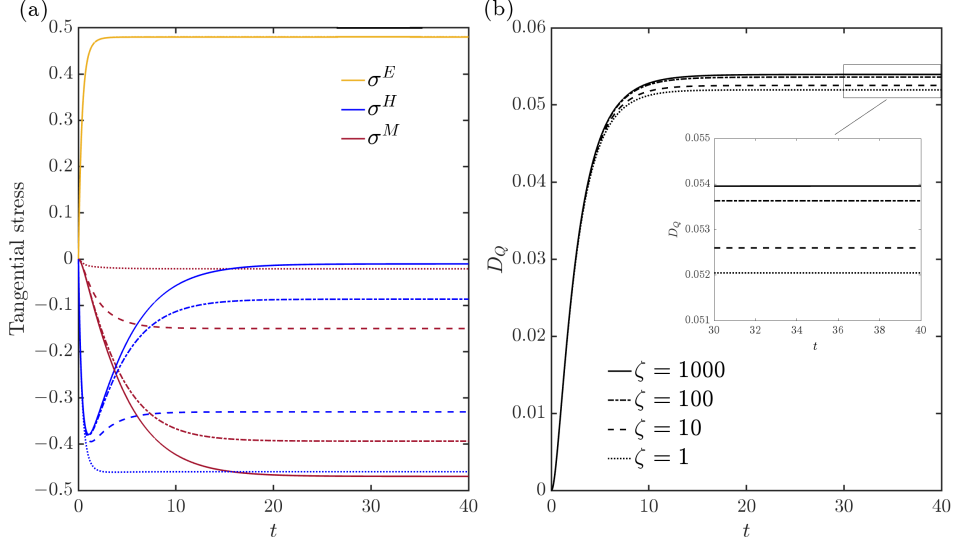


Figure 2: Evolution of (a) the tangential electric (yellow lines), hydrodynamic (blue lines) and Marangoni (dark red lines) stresses and (b) the deformation of a prolate A drop, for  $\zeta = 1$  (dotted lines),  $\zeta = 10$  (dashed lines),  $\zeta = 100$  (dash-dotted lines) and  $\zeta = 1000$  (solid lines). In these figures,  $S = 1/3$ ,  $Q = 1$ ,  $\lambda = 10$ ,  $\text{El} = 0.5$ ,  $\text{Re}_E = 1$ ,  $\text{Ca}_E = 0.2$ .

In Figure 2,  $\text{El} = 0.5$ ,  $\text{Re}_E = 1$ ,  $\text{Ca}_E = 0.2$ , and results are shown for  $\zeta = 1$  (dotted lines),  $\zeta = 10$  (dashed lines),  $\zeta = 100$  (dash-dotted lines), and  $\zeta = 1000$  (solid lines). The electric stress does not change much between these values of  $\zeta$ , suggesting that charge convection does not impact the steady state dipole moment values from equation (3.33) significantly and so the four yellow lines are indistinguishable. When  $\zeta = 1$ , the electric stress shears the fluid into motion and is largely balanced by the resulting hydrodynamic stress, while the Marangoni stress remains relatively weak due to relatively strong surfactant diffusion. Each of  $\sigma^E$ ,  $\sigma^H$ , and  $\sigma^M$  monotonically approaches its steady value with no overshoot as time increases. When  $\zeta = 10$ , the flow is more suppressed than when  $\zeta = 1$ , and the Marangoni stress plays a stronger role in balancing the electric stress than it does when  $\zeta = 1$ , although the hydrodynamic stress is still the stronger of the two. In this case, the hydrodynamic stress slightly overshoots its steady value as the steady surfactant distribution is established. Consistent with previous studies (Nganguia *et al.* 2013; Mandal *et al.* 2016a; Nganguia *et al.* 2019), the flow is suppressed substantially in the cases  $\zeta = 100$  and  $\zeta = 1000$ , and the Marangoni stress plays a much stronger role in balancing the electric stress than does the hydrodynamic stress. The hydrodynamic stress initially increases quickly in response to the electric stresses, convecting surfactant around the drop. This creates surface tension gradients that lead to a relatively strong Marangoni stress that suppresses the flow and decreases the hydrodynamic stress. Figure 2(b) shows the corresponding evolution of the deformation parameter  $D_Q$ , and the inset displays an enlarged view of the steady values. As expected, the deformation increases with  $\zeta$ , and approaches its steady value monotonically as time increases for all of the values of  $\zeta$  shown.

#### 4.3.2. Steady behaviour

Figures 3(a-c) show the dependence of the steady deformation parameter  $D_Q$  of the three drop classes (prolate A, prolate B, and oblate) on  $\zeta$  for four values of  $\text{El}$ . Figure 3(a) shows results for a prolate A drop with  $S = 1/3$ ,  $Q = 1$ , Figure 3(b) shows results for a prolate B

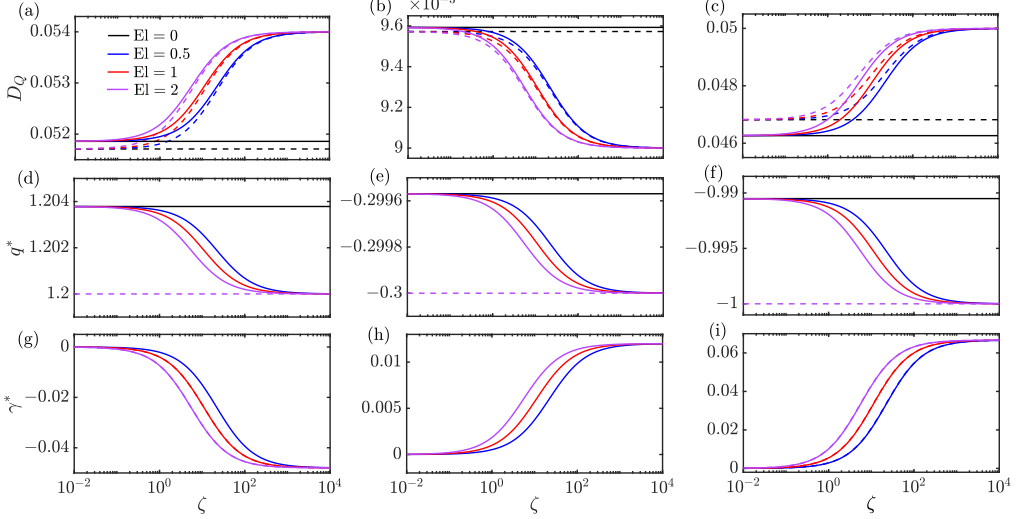


Figure 3: Dependence of the steady deformation parameter  $D_Q$  of (a) a prolate A drop with  $S = 1/3$ ,  $Q = 1$ , (b) a prolate B drop with  $S = 1/3$ ,  $Q = 7/2$ , and (c) an oblate drop with  $S = 1$ ,  $Q = 2$  on  $\zeta$  for  $El = 0$  (black lines), 0.5 (blue lines), 1 (red lines) and 2 (purple lines). The solid lines are the results obtained when retaining charge convection, while the dashed lines are the results obtained when neglecting charge convection. (d–f) show the strength of the surface charge distribution, and (g–i) show the strength of the surface tension variations. In all cases,  $Ca_E = 0.2$ ,  $Re_E = 1$ ,  $\lambda = 10$ .

drop with  $S = 1/3$ ,  $Q = 7/2$ , and Figure 3(c) shows results for an oblate drop with  $S = 1$ ,  $Q = 2$ . In the Taylor regime, the charge distribution  $q$  can be written as

$$q = q^* \cos \theta, \quad (4.23)$$

where  $q^* = 1 - Q + (2 + Q)P_z$ , while the surface tension can be written as

$$\gamma = 1 + \gamma^* P_2(\cos \theta), \quad (4.24)$$

where  $\gamma^* = -Ca_E Q_{zz}^\Gamma$  and  $P_2(\cos \theta) = (3 \cos^2 \theta - 1)/2$  is the second Legendre polynomial. Figures 3(d–f) show  $q^*$ , and Figures 3(g–i) show  $\gamma^*$ , again as functions of  $\zeta$ . In all cases in Figure 3,  $Ca_E = 0.2$ ,  $Re_E = 1$ , and  $\lambda = 10$ . The solid lines are the results obtained when retaining charge convection, while the dashed lines are the results obtained when neglecting charge convection. Black lines correspond to a uniform surface tension drop, i.e.,  $El = 0$ , while the blue, red and purple lines correspond to  $El = 0.5, 1, 2$ , respectively. Note that in Figures 3(g–i), each dashed line lies almost on top of the solid line of the same colour indicating that charge convection has a minimal effect. It is helpful to first examine the dashed lines in Figure 3, which reveal how the drop dynamics depend on  $\zeta$  in the absence of charge convection as studied previously (Nganguia *et al.* 2019). For all three classes of drops, in the limit of strong surfactant diffusion ( $\zeta \rightarrow 0$ ), Figures 3(g–i) show that the surfactant distribution remains uniform regardless of the value of  $El$ , and Figures 3(a–c) show that all drops of each class thus attain the same deformation as a uniform surface tension drop of the relevant class. As the value of  $\zeta$  increases, the effect of varying the elasticity number  $El$  becomes stronger. In the cases of prolate A and oblate drops, the deformation increases with increasing  $\zeta$  or  $El$ , while both trends are reversed for prolate B drops. However, in the case of prolate B and oblate drops, the surface tension at the poles increases with increasing  $\zeta$  or  $El$ , while the surface tension at the poles of a prolate A drop decreases with increasing  $\zeta$  or  $El$ . As we further increase  $\zeta$  towards the limit of zero surfactant diffusion ( $\zeta \rightarrow \infty$ ), the flow is

completely arrested at steady state. Within each class, all drops converge to the same surface tension profile and deformation. Under these circumstances, the surfactant is redistributed by the initial fluid flow until the Marangoni stresses alone balance the tangential electric stresses, and the degree of deformation depends solely on  $\text{Ca}_E$ ,  $S$ , and  $Q$ , as can be seen from (4.14). Note that in Figures 3(d–f), the dashed lines of all four colours lie exactly on top of each other. This is because in the absence of charge convection, the charge distribution is decoupled from the flow and is found by taking the simplified expression for the dipole moment (4.9), yielding

$$q = \left(1 - Q + \frac{(2 + Q)(1 - S)}{1 + 2S}\right) \cos \theta \quad (4.25)$$

for the charge. Thus, the surfactant can affect the charge distribution only through modifying the fluid flow appearing in the convective term in the full dipole evolution equation (3.33). Next, we focus on the solid lines in Figure 3, which correspond to results obtained when charge convection is retained in the model. Previous studies have found that in the absence of surfactants charge convection increases deformation for prolate drops and decreases deformation for oblate drops (Feng 1999; Lanauze *et al.* 2015; Das & Saintillan 2017b). We observe the same effects for surfactant covered drops as well for all values of  $\text{El}$  and  $\zeta$ . This is clearly shown in Figures 3(a,b), in which the solid lines lie above the dashed lines for the prolate drops, and Figure 3(c), in which the solid lines lie below the dashed lines for the oblate drops. As noted in previous studies, charge convection has a greater impact on the deformation of oblate drops than prolate ones. The impact on prolate B drops is particularly small; the hydrodynamic stress, which promotes oblate deformation, is slightly weakened compared to the dominant electric stress, which promotes prolate deformation and is strengthened by charge convection. In the limit of strong surfactant diffusion ( $\zeta \rightarrow 0$ ), the surfactant distribution remains uniform regardless of the value of  $\text{El}$ . The effect of charge convection is strongest in this limit due to the absence of Marangoni stresses. In the limit of zero surfactant diffusion ( $\zeta \rightarrow \infty$ ), the opposite happens and the flow is completely arrested at steady state, hence charge convection has no effect on drop deformation. All surfactant-laden drops of each class attain the same degree of deformation, regardless of the value of  $\text{El}$ .

Figures 3(d–f) show that for prolate A drops, low values of  $\zeta$  lead to a stronger positive charge distribution at the north pole (relative to the direction of the applied field) of the drop, while for oblate and prolate B drops, low values of  $\zeta$  lead to a weaker negative charge distribution at the north pole of the drop. In the prolate A class (Figure 3(d)), the charge distribution is parallel to the field, and since the interfacial velocity carries charges from the equator to the poles, the charge distribution is strengthened by convection. In the prolate B (Figure 3(e)) and oblate classes (Figure 3(f)), the charge distribution is antiparallel to the field, and since the interfacial velocity carries charges from the poles to the equator, the charge distribution is weakened by convection. For all three classes, as  $\zeta$  is increased, the effect of charge convection is diminished because the flow is suppressed, and the value of  $q^*$  converges to that in the absence of convection given in (4.25).

Figures 3(g–i) show that charge convection has very little impact on the surface tension profile for drops in all three classes for the parameter values used. This is explained by the fact that the flow is suppressed when surfactant diffusion is weak, while the surface tension profile is almost uniform regardless of charge convection when surfactant diffusion is strong.

#### 4.4. Quincke regime

In the Quincke regime, the applied electric field exceeds a critical threshold, and the axisymmetric steady state of the drop becomes unstable. When the axisymmetry is broken by

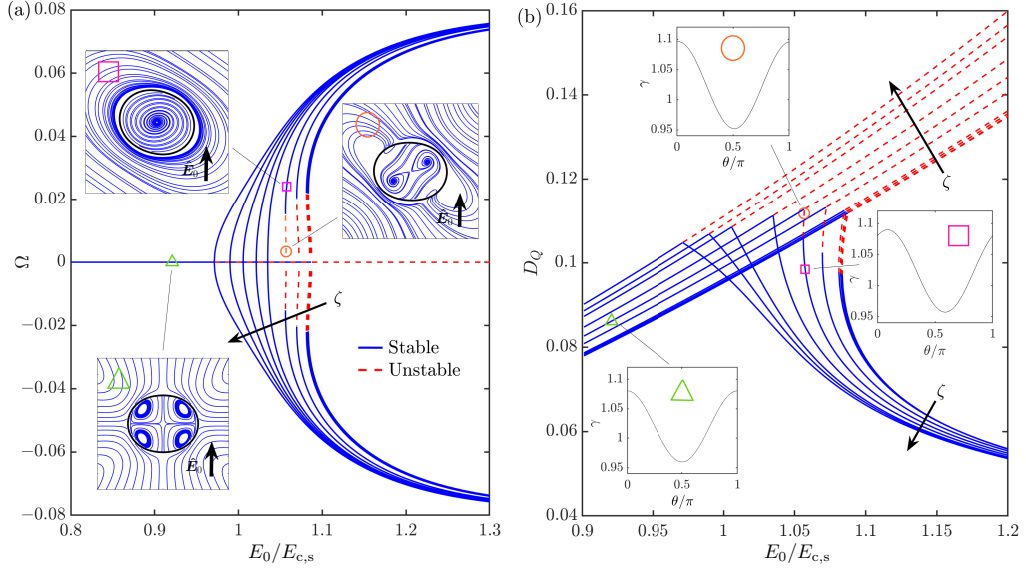


Figure 4: Bifurcation diagrams showing (a) the angular velocity  $\Omega$  and (b) the deformation  $D_Q$  of the drop as functions of the scaled electric field strength  $E_0/E_{c,s}$  for eleven values of  $\zeta = 0.01, 0.1, 0.5, 1, 5, 10, 20, 30, 50, 100, 1000$ , where solid blue lines denote stable solutions and dashed red lines denote unstable solutions. The arrows indicate the directions of increasing  $\zeta$ . The insets in (a) show streamlines around the drop, and the insets in (b) show the corresponding surface tension as a function of  $\theta$ . In all cases,  $E_l = 0.5$  and the other parameter values are those used by Salipante & Vlahovska (2010), given in Table 1.

a perturbation to the drop shape or dipole moment, the drop tilts relative to the applied field and undergoes steady rotation with a constant angular velocity. In this section, we discuss the effects of surfactant on the drop dynamics in the Quincke regime.

#### 4.4.1. Hysteresis

The experiments of Salipante & Vlahovska (2010) demonstrated hysteresis in the angular velocity of drops undergoing Quincke rotation; this behaviour has also been captured theoretically (Peng & Schnitzer 2025; McDougall *et al.* 2025). We first show that the present model reproduces this hysteresis and then examine how surfactant alters it. The bifurcation diagrams in Figure 4 show the angular velocity  $\Omega$  (Figure 4(a)) and the deformation  $D_Q$  (Figure 4(b)) of the drop as functions of the scaled electric field strength  $E_0/E_{c,s}$ . In Figure 4, solid blue lines denote stable solutions and dashed red lines denote unstable solutions. We show solutions for eleven values of  $\zeta = 0.01, 0.1, 0.5, 1, 5, 10, 20, 30, 50, 100, 1000$ . Note that in both Figure 4(a) and 4(b), the curves for  $\zeta = 0.01, 0.1, 0.5, 1$  lie almost on top of one another and so appear as a single thick line. The insets in Figure 4(a) show streamlines around the drop for three different solutions for the case  $\zeta = 10$ , and the insets in Figure 4(b) show the corresponding surface tension as a function of  $\theta$ . In all cases,  $E_l = 0.5$  and the other parameter values are those used by Salipante & Vlahovska (2010), given in Table 1.

Figure 4(a) shows that a stable solution with a straining flow but zero rotational flow (streamlines shown in the inset with the green triangle, with maximum velocity  $0.0058a/\tau_{\text{EHD}}$ ) exists up to a critical electric field strength, at which it becomes unstable and a perturbation to the dipole moment or shape of the drop will lead to steady rotation (streamlines shown in the inset with the pink square, with maximum velocity  $0.045a/\tau_{\text{EHD}}$ ). The present model predicts that hysteresis occurs for the cases in which  $\zeta = 10$  or less,

$\epsilon^+/\epsilon_0$	$\epsilon^-/\epsilon_0$	$\sigma^+$	$\sigma^-$	$\mu^+$	$\mu^-$	$\gamma$	$a$
5.3	3	$4.5 \times 10^{-11}$ S/m	$1.23 \times 10^{-12}$ S/m	0.69 Pa/s	9.73 Pa/s	$4.5 \times 10^{-3}$ N/m	$0.9 \times 10^{-3}$ m

Table 1: Material properties used by Salipante & Vlahovska (2010).  
 $\epsilon_0 = 8.8542 \times 10^{-12}$  F/m is the permittivity of free space.

and that the critical field strength for rotation decreases substantially as  $\zeta$  is increased. The suppression of the straining flow at high values of  $\zeta$  may contribute to this effect; previous work on drops without surfactant have shown that the critical field strength decreases as the strength of the straining flow decreases (Das & Saintillan 2021). Remarkably, for  $\zeta = 100$  and  $\zeta = 1000$ , the model predicts the onset of rotation at a lower critical field strength than that for a solid sphere. In the cases exhibiting hysteresis, the onset of rotation corresponds to a subcritical pitchfork bifurcation, and there is an unstable solution branch on which the drop is tilted and rotates (streamlines shown in the inset with the orange circle, with maximum velocity  $0.011a/\tau_{\text{EHD}}$ ). At higher  $\zeta$ , the pitchfork bifurcation becomes supercritical, and no unstable rotating solution exists.

Figure 4(b) shows the drop deformation corresponding to the angular velocities in Figure 4(a). For the given set of parameters, the drop attains an oblate shape in the Taylor regime. Before Quincke rotation begins, the deformation is greater for higher values of  $\zeta$  than for lower ones, consistent with Figure 3(c), and surfactant accumulates at the drop equator and decreases the surface tension there (see the inset marked with the green triangle), as discussed previously. After the onset of rotation, the deformation decreases due to the rotational flow through the term  $\mathbf{Q}^{\chi f}$ , as discussed in §3.4. The surface tension gradients are largest for solutions on the unstable branch; while increasing the electric field strength increases the surface tension gradients, the rotational component of the flow tends to restore a uniform surfactant distribution through the term  $\mathbf{Q}^{\chi \Gamma}$  in (3.35). This is analogous to the effect of the term  $\mathbf{Q}^{\chi f}$ , which acts to restore a spherical drop shape once rotation begins. In the Quincke regime, the inset in Figure 4(b) marked with the pink square indicates that there is more surfactant at the equator of the drop than at the poles, just as in the Taylor regime. However, counterintuitively, we find that higher values of  $\zeta$  lead to less deformation than do lower values of  $\zeta$ . This is a result of only considering the deformation of the drop in the  $xz$  plane; at high  $\zeta$ , surfactant is transported out of the  $xz$  plane and towards the tips of the drops along the axis of rotation. The convection of surfactant out of the  $xz$  plane is quantified by defining the parameter

$$\eta = \frac{1}{2\pi} \int_0^\pi \Gamma(\theta, \phi = 0) + \Gamma(\theta, \phi = \pi) d\theta - \frac{1}{2\pi} \int_0^\pi \Gamma(\theta, \phi = \pi/2) + \Gamma(\theta, \phi = 3\pi/2) d\theta, \quad (4.26)$$

which measures the difference between the average amount of surfactant in the  $xz$  plane and that in the  $yz$  plane, and takes the simple form

$$\eta = \frac{1}{2} \epsilon \left( Q_{xx}^\Gamma - Q_{yy}^\Gamma \right). \quad (4.27)$$

Figure 5 shows  $\eta$  as a function of  $E_0/E_{c,s}$  for the same parameter values as those used in Figure 4. In the Taylor regime,  $\eta$  is zero because the surfactant distribution is axisymmetric. However, once rotation begins,  $\eta$  becomes negative, indicating that surfactant is moving out

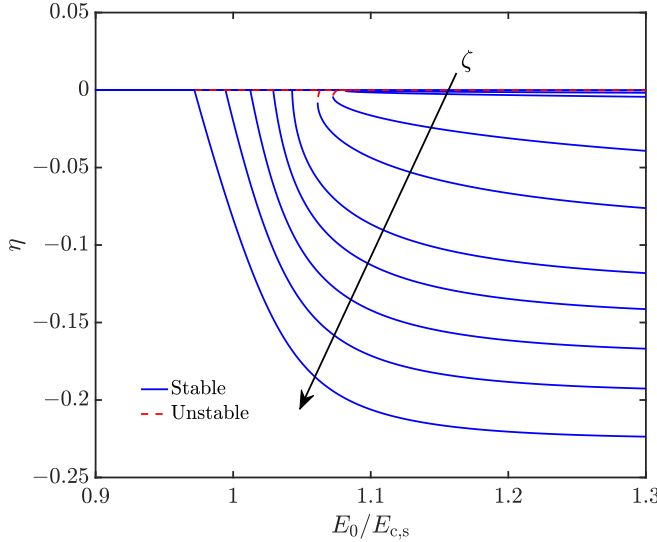


Figure 5: Parameter  $\eta$  given by (4.27) as a function of the scaled electric field strength  $E_0/E_{c,s}$  for the same parameter values as those used in Figure 4. The arrow indicates the direction of increasing  $\zeta$ .

of the  $xz$  plane and accumulating in the  $yz$  plane. This effect, which is stronger for higher values of  $\zeta$ , leads to an increase of the surface tension in the  $xz$  plane, which in turn leads to decreased deformation.

As previously discussed, the strength of the straining flow in the Taylor regime depends on the value of  $\zeta$ . For high values of  $\zeta$ , the flow is suppressed by the Marangoni stresses. However, in the Quincke regime, the surfactant distribution becomes more uniform, so the Marangoni stresses are diminished and the straining flow may be relatively unsuppressed. The strength of the straining flow is quantified by the trace of  $\mathbf{S}^2$ , where  $\mathbf{S} = (\nabla \mathbf{v} + \nabla \mathbf{v}^T)/2$  is the rate-of-strain tensor (Das & Saintillan 2017a). We evaluate  $\text{Tr}(\mathbf{S}^2)$  at the center of the drop,  $\mathbf{r} = \mathbf{0}$ , where it is given by

$$\text{Tr}(\mathbf{S}^2) = 8 \left( q_{xx}^{\phi 2} + q_{zz}^{\phi 2} + q_{xz}^{\phi 2} + q_{xx}^{\phi} q_{zz}^{\phi} \right). \quad (4.28)$$

Figure 6(a) shows  $\text{Tr}(\mathbf{S}^2)$  as a function of  $E_0/E_{c,s}$  for the same parameter values as those used in Figures 4 and 5. As expected, in the Taylor regime, the straining flow becomes weaker for larger values of  $\zeta$ . In the cases corresponding to  $\zeta \leq 30$ , the straining flow is weaker in the Quincke regime than it is in the Taylor regime. This is also the case for a clean drop. However, for the cases  $\zeta = 50$ ,  $\zeta = 100$ , and  $\zeta = 1000$ , the straining flow is stronger in the Quincke regime than it is in the Taylor regime. This is a direct result of the flow suppression effect in the Taylor regime which becomes less prominent in the Quincke regime. As the electric field strength is increased further, the dependence of strength of the straining flow on  $\zeta$  decreases because the surfactant distribution becomes more uniform as a result of the strong rotational flow through the term  $\mathbf{Q}^{\chi\Gamma}$  in (3.35).

The relative strengths of the straining and rotational components of the flow field can be compared by defining the flow assessment parameter (Astarita 1979; Oliveira *et al.* 2009;

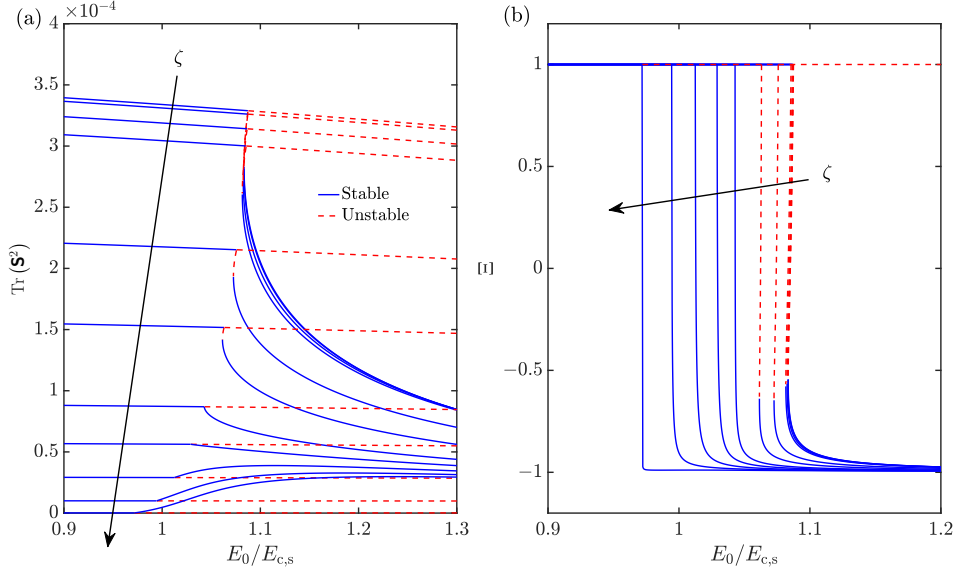


Figure 6: Flow field strength  $\text{Tr}(\mathbf{S}^2)$  given by (4.28) and flow assessment parameter  $\Xi$  given by (4.29) as functions of the scaled electric field strength  $E_0/E_{c,s}$  for the same parameter values as those used in Figures 4 and 5. The arrows indicate the directions of increasing  $\zeta$ .

Poole 2023)

$$\Xi = \frac{\text{Tr}(\mathbf{S}^2) - \text{Tr}(\mathbf{W}^2)}{\text{Tr}(\mathbf{S}^2) + \text{Tr}(\mathbf{W}^2)}, \quad (4.29)$$

where  $\mathbf{W} = (\nabla \mathbf{v} - \nabla \mathbf{v}^T)/2$  is the rate-of-rotation tensor (Das & Saintillan 2017a). Thus,  $\Xi = 1$  corresponds to purely straining flow and  $\Xi = -1$  corresponds to purely rotational flow. Figure 6(b) shows  $\Xi$  as a function of  $E_0/E_{c,s}$  for the same parameter values as in Figures 4 and 5. In the Taylor regime,  $\Xi = 1$  for all values of  $\zeta$ . Even though the straining flow is strongly suppressed for large values of  $\zeta$ , the rotational flow is zero below the critical electric field strength for the bifurcation. Beyond the critical field strength, the value of  $\Xi$  drops towards  $\Xi = -1$ , indicating that the rotational component of the flow is dominant. For large values of  $\zeta$ , this change is particularly sharp because the straining flow is relatively weak in the Quincke regime compared to that for small values of  $\zeta$ , consistent with Figure 6(a). Conversely, the transition from  $\Xi = 1$  towards  $\Xi = -1$  is more gradual for smaller values of  $\zeta$ , for which the straining flow is relatively strong in the Quincke regime. However, as the field strength is increased further, the value of  $\Xi$  converges towards  $-1$  for all values of  $\zeta$ , reflecting the increasing dominance of the rotational flow.

The destabilising effect of a weakly-diffusing surfactant on the Quincke rotation of drops may be useful in practical settings, in which rotation could be induced with a smaller electric field. It is important to bear in mind that this destabilising effect is relative to a uniformly coated drop with constant surface tension  $\gamma_{\text{eq}}$ , rather than to a clean drop with the higher surface tension  $\gamma_0$ . In other words, it is the spatial variations in the surfactant distribution, rather than simply its presence, that provide the effect. However, the critical field for a drop with lower constant surface tension is higher than that of one with higher surface tension, so one might expect this effect to be offset by the global reduction of surface tension arising from the addition of surfactant to a clean drop with surface tension  $\gamma_0$ . However, for the

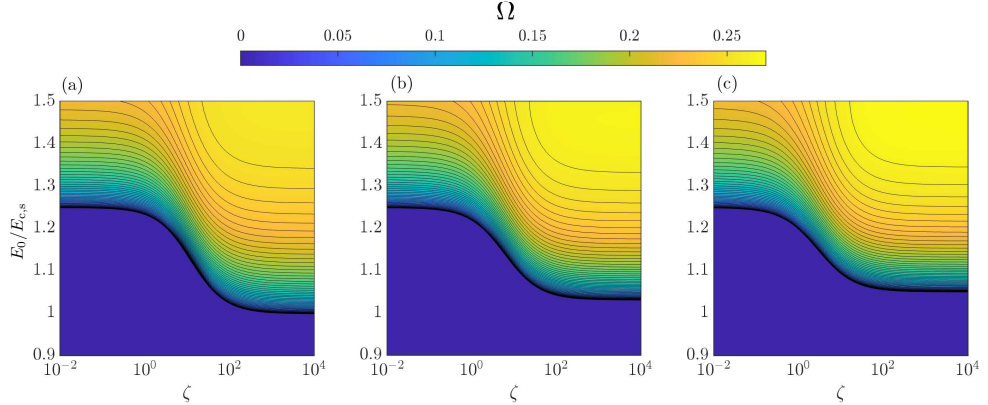


Figure 7: Contour plots showing the angular velocity  $\Omega$  of a drop as a function of the scaled electric field strength  $E_0/E_{c,s}$  and  $\zeta$  for (a)  $El = 0.5$ , (b)  $El = 1$ , and (c)  $El = 2$ . In all cases,  $Q = 5$ ,  $S = 30$ ,  $\lambda = 10$ , and  $0.04 \leq Ca_E \leq 0.1$  and  $0.45 \leq Re_E \leq 1.25$  in the range of field strengths shown.

values  $\gamma_{eq} = 4.5 \times 10^{-3}$  and  $El = 0.5$ , as used here, the corresponding constant surface tension of the same drop without surfactant is  $\gamma_0 = 6.75 \times 10^{-3}$ . Rescaling the capillary number with this surface tension, the critical field for rotation is around  $1.065E_{c,s}$ , while the critical field at  $\zeta = 0$  and a capillary number based on  $\gamma_{eq}$  is around  $1.088E_{c,s}$ . The critical field at  $\zeta = 1000$  and a capillary number based on  $\gamma_{eq}$  is around  $0.97E_{c,s}$ . Hence, the increase in the critical field owing to the global reduction in surface tension is much smaller than the decrease in the critical field due to the spatial variations in surface tension at high  $\zeta$ . Moreover, the present model predicts that this destabilising effect becomes even more significant if  $El$  is decreased further, although this prediction should be interpreted with caution since the present asymptotic analysis formally assumes that  $El = O(1)$ .

#### 4.4.2. Effects of $El$ and $\zeta$ on Quincke rotation

Next, we systematically explore the effects of varying  $El$  and  $\zeta$  on the Quincke rotation of a drop, considering a drop-fluid system for which  $Q = 5$ ,  $S = 30$ , and  $\lambda = 10$ . The model does not predict hysteresis for these parameter values. Figure 7 shows contour plots of the angular velocity  $\Omega$  of the drop as a function of the scaled electric field strength  $E_0/E_{c,s}$  and  $\zeta$  at (a)  $El = 0.5$ , (b)  $El = 1$  and (c)  $El = 2$ . Over the range of field strengths shown, namely  $0.9 \leq E_0/E_{c,s} \leq 1.5$ , the other dimensionless parameters vary in the ranges  $0.04 \leq Ca_E \leq 0.12$  and  $0.45 \leq Re_E \leq 1.25$ . In the limit of strong diffusion (i.e.,  $\zeta \rightarrow 0$ ), the critical field is the same for all three values of  $El$  because the surfactant distribution remains uniform. As  $\zeta$  increases, the critical field decreases and approaches a limiting value as  $\zeta$  becomes large. This behaviour is qualitatively similar at all three values of  $El$ . It is noted that the critical field in the limit of weak diffusion (i.e.,  $\zeta \rightarrow \infty$ ) is highest for  $El = 2$  and lowest for  $El = 0.5$ .

Next, we fix  $\zeta$  and study the effect of changing the scaled electric field strength  $E_0/E_{c,s}$  and the elasticity number  $El$  on the Quincke rotation of the drop. To this end, Figure 8 shows contour plots of the angular velocity  $\Omega$  of the same drop as in Figure 7, but now plotted as a function of  $E_0/E_{c,s}$  and  $El$  at (a)  $\zeta = 0.01$ , (b)  $\zeta = 1$ , and (c)  $\zeta = 1000$ . We denote  $E_{c,d}$  as the value of electric field strength,  $E_0$ , at which the drop starts to rotate. In the case of strong diffusion (Figure 8(a)), the drop behaves essentially like a uniform surface tension drop, and varying  $El$  has little effect on  $E_{c,d}$  or on  $\Omega$ . When diffusion is moderate (Figure 8(b)),

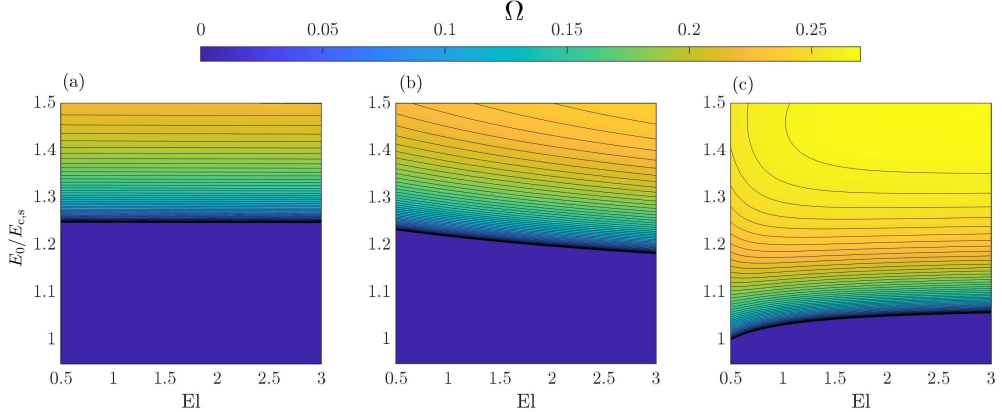


Figure 8: Contour plots showing the angular velocity  $\Omega$  of a drop as a function of the scaled electric field strength  $E_0/E_{c,s}$  and the elasticity number  $El$  for (a)  $\zeta = 0.01$ , (b)  $\zeta = 1$ , and (c)  $\zeta = 1000$ . All the other dimensionless parameters are the same as those used in Figure 7.

increasing  $El$  leads to a decrease in  $E_{c,d}$  and an increase in  $\Omega$ . However, when diffusion is weak (Figure 8(c)),  $E_{c,d}$  instead increases as  $El$  increases. In this case, the dependence of  $\Omega$  on  $El$  depends on the field strength. At field strengths only just strong enough to induce rotation (i.e.,  $E_0/E_{c,s}$  less than approximately 1.1 in Figure 8(c)), an increase in  $El$  leads to a decrease in  $\Omega$ . At slightly greater field strengths (i.e.,  $E_0/E_{c,s}$  around 1.2 in Figure 8(c)), an increase in  $El$  initially leads to an increase in  $\Omega$ , before the trend reverses and further increases in  $El$  lead to a decrease in  $\Omega$ . At relatively large field strengths (i.e.,  $E_0/E_{c,s}$  greater than approximately 1.3 in Figure 8(c)), an increase in  $El$  initially leads to an increase in  $\Omega$ , before the effect vanishes and  $\Omega$  becomes insensitive to further increases in  $El$ .

The relationship between the elasticity number  $El$  and the critical electric field strength  $E_{c,d}$  can be explored further using the linear stability analysis described in §4.1. Figure 9 shows the critical field strengths for rotation of a drop scaled by that for a solid sphere  $E_{c,d}/E_{c,s}$  as functions of  $El$  for thirty logarithmically spaced values of  $\zeta$  between  $10^{-2}$  and  $10^4$ , specifically for  $\zeta = 10^{(-2+6n/29)}$  for  $n = 0, 1, 2, \dots, 28, 29$ . The curves in Figure 9 generated from the linear stability analysis are the same as the marginal curves in Figure 8 that separate the Taylor and Quincke regimes. Figure 9(a) shows results for  $\lambda = 10$ , and Figure 9(b) shows results for  $\lambda = 50$ . The other parameters are the same as those used in Figures 7 and 8. Figure 9 indicates that the effect of the surfactant is destabilising over the full range shown of  $0.5 \leq El \leq 3$ , and that the effect is more pronounced for  $\lambda = 10$  than for  $\lambda = 50$ . It also shows that increasing  $El$  leads to a decrease in  $E_{c,d}/E_{c,s}$  at lower values of  $\zeta$ , and that the trend reverses at higher values of  $\zeta$ , consistent with the results shown in Figure 8.

Next, we focus our attention on the effects of varying  $\zeta$  and the elasticity number  $El$  at fixed electric field strengths close to the critical field for Quincke rotation. Firstly, Figure 10 shows contour plots of the angular velocity  $\Omega$  of the drop as a function of  $\zeta$  and  $El$  for eight field strengths increasing in increments of 0.005 from  $E_0/E_{c,s} = 1.045$  (Figure 10(a)) to  $E_0/E_{c,s} = 1.080$  (Figure 10(h)). The inset in Figure 10(a) displays the marginal curves between the axisymmetric and rotational solution regions as functions of  $El$  for (a)  $E_0/E_{c,s} = 1.045$ , (b)  $E_0/E_{c,s} = 1.05$ , and (c)  $E_0/E_{c,s} = 1.055$  using a logarithmic scale. At each field strength shown, the angular velocity is greatest for the highest values of  $\zeta$  and the lowest values of  $El$  shown. As in Figure 7, the critical field strength  $E_{c,d}/E_{c,s}$  at which rotation

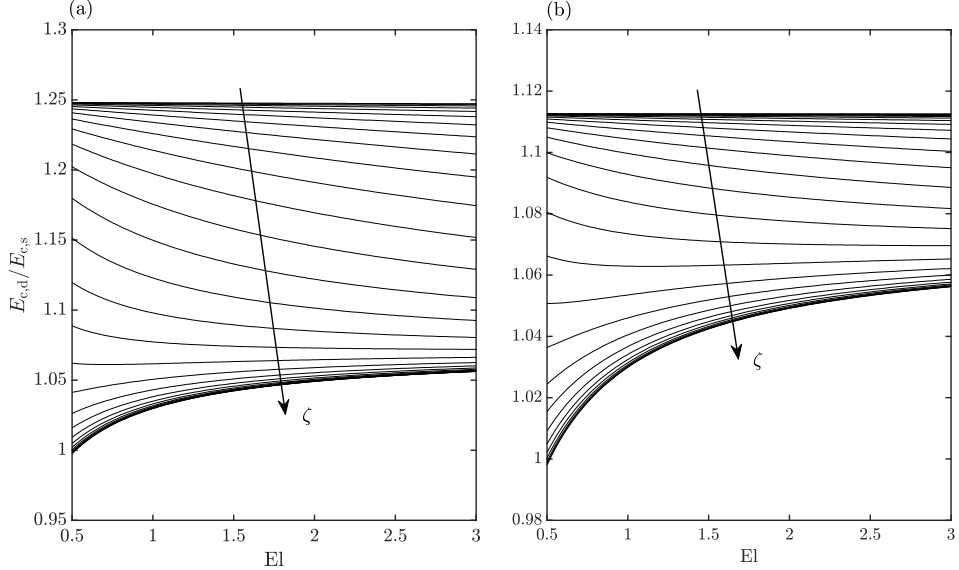


Figure 9: Scaled critical electric field strengths for the onset of Quincke rotation of a drop  $E_{c,d}/E_{c,s}$  as functions of  $El$  for thirty logarithmically spaced values of  $\zeta$  between  $10^{-2}$  and  $10^4$ , specifically for  $\zeta = 10^{(-2+6n/29)}$  for  $n = 0, 1, 2, \dots, 28, 29$ . (a) shows results for  $\lambda = 10$ , and (b) shows results for  $\lambda = 50$ . The dimensionless parameters are the same as those used in Figures 7 and 8.

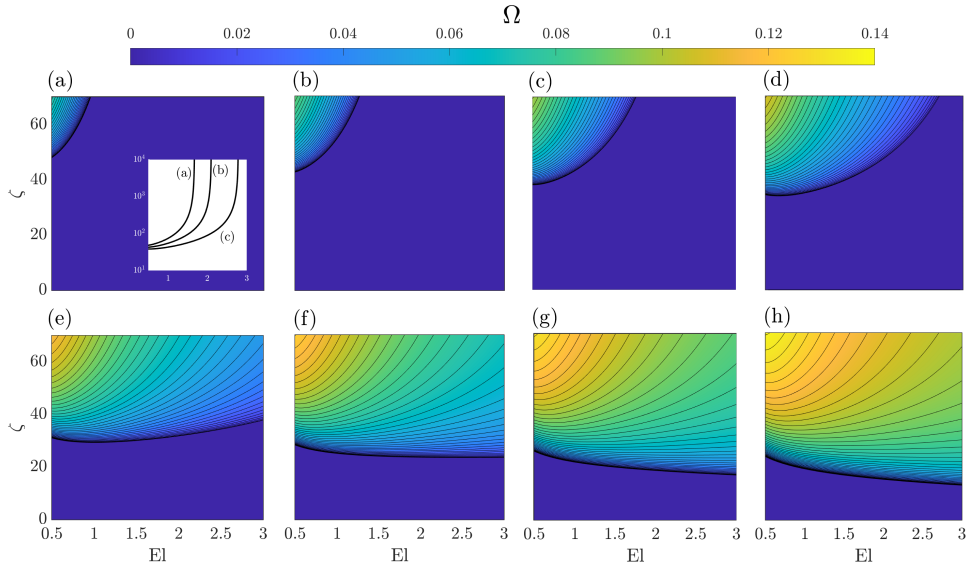


Figure 10: Contour plots showing the angular velocity  $\Omega$  of a drop as a function of  $\zeta$  and the elasticity number  $El$  for eight electric field strengths  $E_0/E_{c,s} = 1.045, 1.05, \dots, 1.075, 1.08$ . All the other dimensionless parameters are the same as those used in Figures 7, 8, and 9. The inset in (a) displays the marginal curves between the axisymmetric and rotational solution regions as functions of  $El$  for (a)  $E_0/E_{c,s} = 1.045$ , (b)  $E_0/E_{c,s} = 1.05$ , and (c)  $E_0/E_{c,s} = 1.055$  using a logarithmic scale.

occurs for a given value of  $El$  is decreased as  $\zeta$  is increased. Hence, for a given field strength that is greater than the critical field strength for rotation in the limit  $\zeta \rightarrow \infty$  (i.e., the limit of weak surfactant diffusion) but smaller than that in the limit  $\zeta \rightarrow 0$  (i.e., the limit of strong surfactant diffusion), there exists a critical value of  $\zeta$  at which the drop becomes unstable and Quincke rotation occurs. This critical value corresponds to the marginal curves between the axisymmetric and rotational solution regions. At the lowest field strength considered,  $E_0/E_{c,s} = 1.045$  (Figure 10(a)), the critical value increases sharply as  $El$  is increased. As shown in the inset, the critical value diverges as  $El$  approaches  $El \approx 1.67$ . Above  $El \approx 1.67$ , the field is too weak to induce rotation at any value of  $\zeta$ . The critical values at the second and third field strengths shown,  $E_0/E_{c,s} = 1.05$  and  $E_0/E_{c,s} = 1.055$  (Figures 10(b) and (c)), diverge as the elasticity number approaches  $El \approx 2.1$  and  $El \approx 2.78$ , respectively. For field strengths at or above that shown in Figure 10(d), corresponding to  $E_0/E_{c,s} = 1.06$ , the critical value of  $\zeta$  is smaller than  $\zeta = 40$  for all values of  $El$  in the range shown. Furthermore, when the field strength is at or above  $E_0/E_{c,s} = 1.07$ , the critical value of  $\zeta$  decreases with increasing  $El$  in the range shown. Hence, the critical value of  $\zeta$  and the angular velocity of the drop are significantly more sensitive to changes in the field strength for  $El = 3$  than they are for  $El = 0.5$ . On the other hand, the contour lines indicate that for the field strengths shown,  $\Omega$  is more sensitive to changes in  $\zeta$  when  $El = 0.5$  than when  $El = 3$ .

Figure 11 shows the scaled critical electric field strength for Quincke rotation of a drop  $E_{c,d}/E_{c,s}$  (Figure 11(a)), angular velocity  $\Omega$  (Figures 11(b) and (c)), straining flow strength  $\text{Tr}(\mathbf{S}^2)$  ((d) and (e)), and deformation parameter  $D_Q$  (Figures 11(f) and (g)) as functions of  $\zeta$  for  $El = 0.5$  (purple dash-dotted lines), 1 (black dotted lines), 2 (red dashed lines), and 3 (blue solid lines). Figures 11(b), (d) and (f) correspond to  $E_0/E_{c,s} = 1.1$ , while Figures 11(c), (e) and (g) correspond to  $E_0/E_{c,s} = 1.05$ . We again use  $Q = 5$  and  $S = 30$ , and the other relevant parameters are  $\text{Ca}_E = 0.06$  and  $\text{Re}_E = 0.6$  at  $E_0/E_{c,s} = 1.05$ , and  $\text{Ca}_E = 0.07$  and  $\text{Re}_E = 0.67$  at  $E_0/E_{c,s} = 1.1$ . These field strengths are marked by the thin horizontal lines in Figure 11(a), in which the green line marks  $E_0/E_{c,s} = 1.05$  and the black line marks  $E_0/E_{c,s} = 1.1$ . The predicted critical values of  $\zeta$  at the given field strengths are given by the  $\zeta$  coordinates of the intersections of these horizontal lines and the solution curves in Figure 11(a), and are denoted in the relevant subplots by the thin vertical green and black lines. The critical field strengths  $E_{c,d}/E_{c,s}$  shown in Figure 11(a) are obtained from the linear stability analysis described in §4.1, and are the same as the marginal curves separating the Taylor and Quincke regimes in Figure 7. Similarly, Figures 11(b) and (c) correspond to horizontal slices of Figure 7. At  $E_0/E_{c,s} = 1.05$ , the critical value of  $\zeta$  is lower for lower values of  $El$  than for higher ones, and indeed no bifurcation occurs at all for the case  $El = 3$ . However, the trend reverses at  $E_0/E_{c,s} = 1.1$ , and the critical value of  $\zeta$  decreases as  $El$  is increased. Figures 11(b) and (c) show that at both of these field strengths, the angular velocity is larger for lower values of  $El$  than for higher ones as  $\zeta$  grows large, even though drops with higher  $El$  destabilise at lower values of  $\zeta$  at  $E_0/E_{c,s} = 1.1$ . Figures 11(d) and (e) show that as  $\zeta$  is increased, the straining flow is weakened due to the increasing Marangoni stresses. However, beyond the critical value of  $\zeta$ , the straining flow is strengthened with further increases in  $\zeta$  for the cases  $El = 1, 2$ , and  $3$  at  $E_0/E_{c,s} = 1.1$  (Figure 11(d)) and for the cases  $El = 1$  and  $2$  at  $E_0/E_{c,s} = 1.05$  (Figure 11(e)). On the other hand, for  $El = 0.5$ , the straining flow continues decreasing in strength as  $\zeta$  is increased beyond its critical value at both field strengths considered. Figures 11(f) and (g) show that in the limit of strong diffusion (i.e., in the limit  $\zeta \rightarrow 0$ ), in which all of the drops are in the Taylor regime, all of the drops have the same deformation at a given field strength because the surfactant distribution remains uniform in all cases, as is the case for the results shown in Figure 3. As  $\zeta$  is increased, the deformation increases due to the accumulation of surfactant around the equator, with the deformation becoming greater for greater values of  $El$ . However, above the critical value

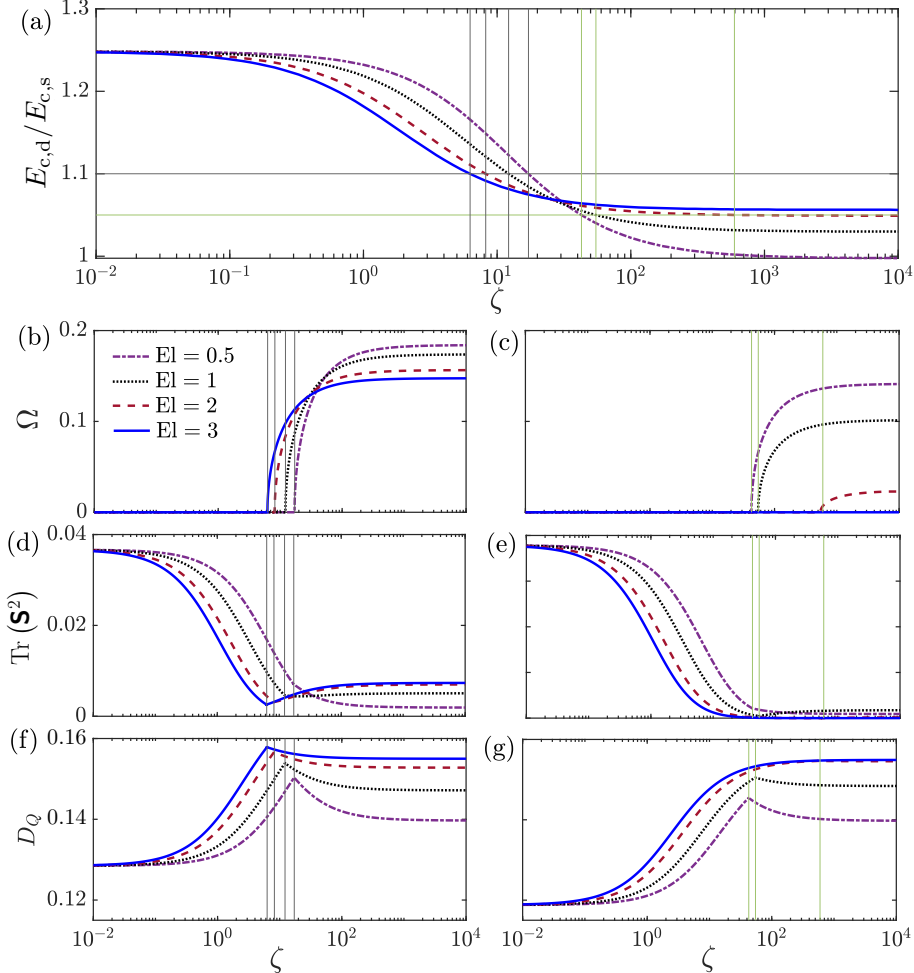


Figure 11: (a) Scaled critical electric field strength for Quincke rotation of a drop  $E_{c,d}/E_{c,s}$ , (b,c) angular velocity  $\Omega$ , (d,e) straining flow strength  $\text{Tr}(\mathbf{S}^2)$ , and (f,g) deformation parameter  $D_Q$  as functions of  $\zeta$  for  $\text{El} = 0.5$  (purple dash-dotted lines), 1 (black dotted lines), 2 (red dashed lines), and 3 (blue solid lines). (b), (d) and (f) correspond to  $E_0/E_{c,s} = 1.1$ , while (c), (e) and (g) correspond to  $E_0/E_{c,s} = 1.05$ . These field strengths are indicated by the thin black and green horizontal lines in (a), respectively, and the predicted critical values of  $\zeta$  are denoted in the relevant subplots by the thin vertical green and black lines. We again use  $Q = 5$  and  $S = 30$ , and the other relevant parameters are  $\text{Ca}_E = 0.06$  and  $\text{Re}_E = 0.6$  at  $E_0/E_{c,s} = 1.05$ , and  $\text{Ca}_E = 0.07$  and  $\text{Re}_E = 0.67$  at  $E_0/E_{c,s} = 1.1$ .

of  $\zeta$ , the deformation begins to decrease as  $\zeta$  increases. The reduction of the deformation in the Quincke regime becomes more pronounced as  $\text{El}$  is decreased. Thus, in the limit of zero diffusion (i.e., in the limit  $\zeta \rightarrow \infty$ ) the deformation of surfactant-laden oblate drops increases as  $\text{El}$  is increased in the Quincke regime, unlike in the Taylor regime, in which the deformation is the same for all values of  $\text{El}$ .

## 5. Conclusions

In the present work, we have described a small-deformation theory for a leaky dielectric drop coated with a dilute monolayer of insoluble apolar surfactant and subjected to a uniform DC electric field. The novelty of our work lies in the retention of charge convection in the transport equation for the surface charge, which allows the theory to capture Quincke rotation. We have examined the combined effects of surfactant and charge convection on drop deformation in the Taylor regime, and found that the two effects work cooperatively to promote increased deformation of prolate A drops, but that they work antagonistically in the cases of prolate B and oblate drops. Our theory predicts that the presence of a weakly-diffusing surfactant can eliminate the hysteresis that occurs in the angular velocity of drops undergoing Quincke rotation and can significantly lower the critical electric field strength for the onset of rotation from that for a drop of constant surface tension. We find that for an oblate drop in the Quincke regime, the surfactant is transported out of the rotational plane and accumulates at the tips of the drop along the axis of rotation.

A linear stability analysis of the system reveals that for strongly-diffusing surfactants (i.e., for low values of  $\zeta$ ), an increase in El leads to an decrease in the critical electric field strength for the onset of rotation  $E_{c,d}$ , while the opposite is true for weakly-diffusing surfactants (i.e., for high values of  $\zeta$ ). We have explored the effects of varying  $\zeta$  and the elasticity number El on the deformation and angular velocity of an oblate drop at fixed electric field strengths. We find that larger values of El lead to larger deformation than do smaller ones across the whole range of  $\zeta$  studied, and smaller values of El lead to larger angular velocity than do larger ones in the limit of large  $\zeta$ . At intermediate values of  $\zeta$ , the relationship between the angular velocity and El depends on the field strengths: at larger field strengths, drops with larger values of El begin rotating at a smaller critical value of  $\zeta$  than do drops with smaller values of El. At smaller field strengths, the opposite is true, and drops with smaller values of El begin rotating at smaller critical values of  $\zeta$ , while drops with larger values of El may not rotate at all, even in the limit of large  $\zeta$ .

While the linearisation of the Langmuir equation (2.12) is convenient for the spherical harmonic representation used in the present theory, it restricts the present theory to dilute concentrations of surfactant, and the theory thus fails to capture some of the qualitative features of surfactant effects at higher concentrations as found by Nganguia *et al.* (2019). For example, their spheroidal theory predicts that the deformation of prolate A drops decreases and that of prolate B drops increases with increasing surfactant concentration at low  $\zeta$ , while the opposite is true at high  $\zeta$ . However, since the present theory is valid for dilute concentrations, this complexity is lost. Full simulations using a finite or boundary element method may be used to explore the effects of nondilute concentrations. Additionally, the small-deformation theory of an isolated drop developed here is a first step towards understanding the electrorheology of emulsions of drops covered with surfactants, which could be achieved either using particle-based simulations (Das & Saintillan 2023) or by coarse-graining the governing equations (Vlahovska 2011). Finally, the framework developed here can be extended to incorporate interfacial rheological effects, such as surface viscosities (Scriven 1960; Mandal & Chakraborty 2017; Nganguia *et al.* 2023), while retaining charge convection in three dimensions, to study their influence on Quincke rotation.

**Supplementary data.** MATLAB codes to reproduce the figures in this article are available in the Supplementary Material.

**Funding.** The authors gratefully acknowledge the financial support of the University of Strathclyde in the form of a Research Excellence Award.

**Declaration of interests.** The authors report no conflict of interest.

**Author ORCIDs.** M. A. McDougall, <https://orcid.org/0009-0005-2967-9437>;  
S. K. Wilson, <https://orcid.org/0000-0001-7841-9643>;  
D. Das, <https://orcid.org/0000-0003-2365-4720>

## Appendix A.

In this appendix, for completeness, we give the elements of the Jacobian matrix in the linear system of equations (4.7).

$$\begin{aligned}
J_{11} = & -\frac{1+2S}{S(2+Q)\text{Re}_E} - \frac{1-Q}{2(2+Q)} + \frac{(1-Q)(1-4Q)}{30(3+2\lambda)(2+Q)} \\
& + P_{0,z} \left( -\frac{1}{2} + \frac{1}{5(3+2\lambda)} \left[ \frac{5-8Q}{6} - \frac{9(14+11\lambda)(1-Q)}{(16+19\lambda)(2+Q)} \right] \right) \\
& + P_{0,z}^2 \frac{2}{15(3+2\lambda)} \left( 2+Q - \frac{9(14+11\lambda)}{16+19\lambda} \right) \\
& + Q_{0,xx}^f \frac{6(14+11\lambda)}{5(16+19\lambda)(3+2\lambda)(1+2S)^2} - Q_{0,xx}^\Gamma \frac{2(8+5\lambda)\epsilon E l}{\text{Ca}_E(16+19\lambda)(3+2\lambda)}, \tag{A 1}
\end{aligned}$$

$$J_{15} = \left( P_{0,z} + \frac{1-Q}{2+Q} \right) \frac{6(14+11\lambda)}{5(16+19\lambda)(3+2\lambda)(1+2S)^2}, \tag{A 2}$$

$$J_{18} = -\left( P_{0,z} + \frac{1-Q}{2+Q} \right) \frac{2(8+5\lambda)\epsilon E l}{\text{Ca}_E(16+19\lambda)(3+2\lambda)}, \tag{A 3}$$

$$\begin{aligned}
J_{22} = & -\frac{1+2S}{S(2+Q)\text{Re}_E} - \frac{6(1-Q^2)}{15(3+2\lambda)(2+Q)} \\
& + P_{0,z} \frac{4}{15(3+2\lambda)} \left( -3Q - \frac{9(14+11\lambda)(1-Q)}{(16+19\lambda)(2+Q)} \right) \\
& + P_{0,z}^2 \frac{2}{5(3+2\lambda)} \left[ 2+Q - \frac{9(14+11\lambda)}{16+19\lambda} \right] \\
& + Q_{0,zz}^f \frac{6(14+11\lambda)}{5(16+19\lambda)(3+2\lambda)(1+2S)^2} - Q_{0,zz}^\Gamma \frac{2(8+5\lambda)\epsilon E l}{\text{Ca}_E(16+19\lambda)(3+2\lambda)}, \tag{A 4}
\end{aligned}$$

$$J_{24} = J_{15}, \quad J_{27} = J_{18}, \tag{A 5}$$

$$J_{32} = -\frac{1+2Q}{3\delta(3+2\lambda)} - \frac{2}{3\delta(3+2\lambda)} \left( \frac{45(1+\lambda)}{16+19\lambda} - (2+Q) \right) P_{0,z}, \tag{A 6}$$

$$J_{33} = -\frac{30(1+\lambda)}{\delta(16+19\lambda)(3+2\lambda)(1+2S)^2}, \tag{A 7}$$

$$J_{36} = \frac{2(4+\lambda)\epsilon E l}{\text{Ca}_E \delta(16+19\lambda)(3+2\lambda)}, \tag{A 8}$$

$$J_{42} = -2J_{32}, \quad J_{44} = J_{33}, \quad J_{47} = J_{36}, \tag{A 9}$$

$$J_{51} = -\frac{3}{2}J_{32} + \frac{1}{2} \left( Q_{0,xx}^f - Q_{0,zz}^f \right), \tag{A 10}$$

$$J_{55} = J_{44} = J_{33}, \quad J_{58} = J_{47} = J_{36}, \tag{A 11}$$

$$J_{62} = -\frac{(1+2Q)}{3\epsilon(3+2\lambda)} + \frac{2(68+47\lambda+Q(16+19\lambda))}{3\epsilon(16+19\lambda)(3+2\lambda)} P_{0,z}, \tag{A 12}$$

$$J_{63} = \frac{6(4+\lambda)}{\epsilon(16+19\lambda)(3+2\lambda)(1+2S)^2}, \tag{A 13}$$

$$J_{66} = -\left( \frac{6}{\zeta \text{Re}_E} + \frac{2(32+23\lambda)\epsilon E l}{\text{Ca}_E(16+19\lambda)(3+2\lambda)} \right), \tag{A 14}$$

$$J_{72} = -2J_{62}, \quad J_{74} = J_{63}, \quad J_{77} = J_{66}, \quad (A\,15)$$

$$J_{81} = -\frac{3}{2}J_{62} + \frac{1}{2}\left(Q_{0,xx}^{\Gamma} - Q_{0,zz}^{\Gamma}\right), \quad (A\,16)$$

$$J_{85} = J_{74} = J_{63}, \quad J_{88} = J_{77} = J_{66}. \quad (A\,17)$$

## REFERENCES

AJAYI, O. O. 1978 A note on Taylor's electrohydrodynamic theory. *Proc. R. Soc. Lond. A* **364** (1719), 499–507.

ALLAN, R. S. & MASON, S. G. 1961 Effects of electric fields on coalescence in liquid + liquid systems. *Trans. Faraday Soc.* **57**, 2027–2040.

ALLAN, R. S. & MASON, S. G. 1962 Particle behaviour in shear and electric fields I. Deformation and burst of fluid drops. *Proc. R. Soc. Lond. A* **267** (1328), 45–61.

ASTARITA, G. 1979 Objective and generally applicable criteria for flow classification. *J. Non-Newton. Fluid Mech.* **6** (1), 69–76.

BANDOPADHYAY, A., MANDAL, S., KISHORE, N.K. & CHAKRABORTY, S. 2016 Uniform electric-field-induced lateral migration of a sedimenting drop. *J. Fluid Mech.* **792**, 553–589.

BARTHÈS-BIESEL, D. & ACRIVOS, A. 1973 Deformation and burst of a liquid droplet freely suspended in a linear shear field. *J. Fluid Mech.* **61** (1), 1–22.

BARTOK, W. & MASON, S. G. 1959 Particle motions in sheared suspensions: VIII. Singlets and doublets of fluid spheres. *J. Colloid Sci.* **14** (1), 13–26.

BASU, H. S., JENA, S. K. & KONDARAJU, S. 2024 Role of surface charge convection on oblate droplets in different conductivity regimes. *Phys. Fluids* **36** (10), 102125.

BAYGENTS, J. C. & SAVILLE, D. A. 1991 Electrophoresis of drops and bubbles. *J. Chem. Soc. Faraday Trans. 87* (12), 1883–1898.

BRICARD, A., CAUSSIN, J.-B., DAS, D., SAVOIE, C., CHIKKADI, V., SHITARA, K., CHEPIZHKO, O., PERUANI, F., SAINTILLAN, D. & BARTOLO, D. 2015 Emergent vortices in populations of colloidal rollers. *Nat. Commun.* **6** (1), 7470.

BRICARD, A., CAUSSIN, J.-B., DESREUMAUX, N., DAUCHOT, O. & BARTOLO, D. 2013 Emergence of macroscopic directed motion in populations of motile colloids. *Nature* **503** (7474), 95–98.

BUREIKO, A., TRYBALA, A., KOVALCHUK, N. & STAROV, V. 2015 Current applications of foams formed from mixed surfactant–polymer solutions. *Adv. Colloid Interface Sci.* **222**, 670–677.

CHAFFEY, C. E. & BRENNER, H. 1967 A second-order theory for shear deformation of drops. *J. Colloid Interface Sci.* **24** (2), 258–269.

COX, R. G. 1969 The deformation of a drop in a general time-dependent fluid flow. *J. Fluid Mech.* **37** (3), 601–623.

DAS, D. & LAUGA, E. 2019 Active particles powered by Quincke rotation in a bulk fluid. *Phys. Rev. Lett.* **122** (19), 194503.

DAS, D. & SAINTILLAN, D. 2017a Electrohydrodynamics of viscous drops in strong electric fields: numerical simulations. *J. Fluid Mech.* **829**, 127–152.

DAS, D. & SAINTILLAN, D. 2017b A nonlinear small-deformation theory for transient droplet electrohydrodynamics. *J. Fluid Mech.* **810**, 225–253.

DAS, D. & SAINTILLAN, D. 2021 A three-dimensional small-deformation theory for electrohydrodynamics of dielectric drops. *J. Fluid Mech.* **914**, A22.

DAS, D. & SAINTILLAN, D. 2023 On the absence of collective motion in a bulk suspension of spontaneously rotating dielectric particles. *Soft Matter* **19** (35), 6825–6837.

DAVIS, R. E. & ACRIVOS, A. 1966 The influence of surfactants on the creeping motion of bubbles. *Chem. Eng. Sci.* **21** (8), 681–685.

DONG, Q. & SAU, A. 2023 Unsteady electrorotation of a viscous drop in a uniform electric field. *Phys. Fluids* **35** (4), 047116.

EGGLETON, C. D., PAWAR, Y. P. & STEBE, K. J. 1999 Insoluble surfactants on a drop in an extensional flow: a generalization of the stagnated surface limit to deforming interfaces. *J. Fluid Mech.* **385**, 79–99.

EGGLETON, C. D. & STEBE, K. J. 1998 An adsorption–desorption-controlled surfactant on a deforming droplet. *J. Colloid Interface Sci.* **208** (1), 68–80.

Eow, J. S. & GHADIRI, M. 2003a Drop–drop coalescence in an electric field: the effects of applied electric field and electrode geometry. *Colloids Surf. A: Physicochem. Eng. Asp.* **219** (1-3), 253–279.

Eow, J. S. & GHADIRI, M. 2003b Motion, deformation and break-up of aqueous drops in oils under high electric field strengths. *Chem. Eng. Process.: Process Intensif.* **42** (4), 259–272.

ESMAEELI, A. & BEHJATIAN, A. 2020 Transient electrohydrodynamics of a liquid drop at finite Reynolds numbers. *J. Fluid Mech.* **893**, A26.

ESMAEELI, A. & SHARIFI, P. 2011 Transient electrohydrodynamics of a liquid drop. *Phys. Rev. E* **84** (3), 036308.

FENG, J. Q. 1999 Electrohydrodynamic behaviour of a drop subjected to a steady uniform electric field at finite electric Reynolds number. *Proc. R. Soc. Lond. A* **455** (1986), 2245–2269.

FENG, J. Q. 2002 A 2D electrohydrodynamic model for electrorotation of fluid drops. *J. Colloid Interface Sci.* **246** (1), 112–121.

FIROUZNIA, M., BRYNGELSON, S. H. & SAINTILLAN, D. 2023 A spectral boundary integral method for simulating electrohydrodynamic flows in viscous drops. *J. Comput. Phys.* **489**, 112248.

FITZGERALD, E., CLAVAUD, C., DAS, D., LENTON, I. C. D. & WAITUKAITIS, S. R. 2025 Rolling at right angles: magnetic anisotropy enables dual-anisotropic active matter. *arXiv preprint arXiv:2508.05643*.

FLUMERFELT, R. W. 1980 Effects of dynamic interfacial properties on drop deformation and orientation in shear and extensional flow fields. *J. Colloid Interface Sci.* **76** (2), 330–349.

GREENSPAN, H. P. 1977 On the deformation of a viscous droplet caused by variable surface tension. *Stud. Appl. Math.* **57** (1), 45–58.

GRIFFITH, R. M. 1962 The effect of surfactants on the terminal velocity of drops and bubbles. *Chem. Eng. Sci.* **17** (12), 1057–1070.

HA, J.-W. & YANG, S.-M. 1995 Effects of surfactant on the deformation and stability of a drop in a viscous fluid in an electric field. *J. Colloid Interface Sci.* **175** (2), 369–385.

HABER, S. & HETSRONI, G. 1972 Hydrodynamics of a drop submerged in an unbounded arbitrary velocity field in the presence of surfactants. *Appl. Sci. Res.* **25** (1), 215–233.

HAN, E., ZHU, L., SHAEVITZ, J. W. & STONE, H. A. 2021 Low-Reynolds-number, biflagellated Quincke swimmers with multiple forms of motion. *Proc. Natl. Acad. Sci.* **118** (29), e2022000118.

HAN, Y., KOPLIK, J. & MALDARELLI, C. 2022 Surfactant and dilatational viscosity effects on the deformation of liquid droplets in an electric field. *J. Colloid Interface Sci.* **607** (1), 900–911.

HAPPEL, J. & BRENNER, H. 1983 *Low Reynolds number hydrodynamics: with special applications to particulate media*. Martinus Nijhoff.

HE, H., SALIPANTE, P. F. & VLAHOVSKA, P. M. 2013 Electrorotation of a viscous droplet in a uniform direct current electric field. *Phys. Fluids* **25** (3), 032106.

JONES, T. B. 1984 Quincke rotation of spheres. *IEEE Trans. Ind. Appl.* **IA-20** (4), 845–849.

KIM, S. & KARRILA, S. J. 1991 *Microhydrodynamics: principles and selected applications*. Butterworth-Heinemann.

KOVALCHUK, N. M. & SIMMONS, M. J. H. 2021 Surfactant-mediated wetting and spreading: Recent advances and applications. *Curr. Opin. Colloid Interface Sci.* **51**, 101375.

KRALOVA, I. & SJÖBLOM, J. 2009 Surfactants used in food industry: a review. *J. Disper. Sci. Technol.* **30** (9), 1363–1383.

LAC, E. & HOMSY, G. M. 2007 Axisymmetric deformation and stability of a viscous drop in a steady electric field. *J. Fluid Mech.* **590**, 239–264.

LAMB, H. 1932 *Hydrodynamics*, 6th edn. Cambridge University Press.

LAMPA, A. S. 1906 Dielectric hysteresis. *Sitzungberichte d. k. Akademie der Wissenschaften* **115**, 1657–1690.

LANAUZE, J. A., WALKER, L. M. & KHAIR, A. S. 2015 Nonlinear electrohydrodynamics of slightly deformed oblate drops. *J. Fluid Mech.* **774**, 245–266.

LEVICH, V. G. 1962 *Physicochemical Hydrodynamics*. Prentice-Hall.

LÓPEZ-HERRERA, J. M., POPINET, S. & HERRADA, M. A. 2011 A charge-conservative approach for simulating electrohydrodynamic two-phase flows using volume-of-fluid. *J. Comput. Phys.* **230** (5), 1939–1955.

LOTYA, M., KING, P. J., KHAN, U., DE, S. & COLEMAN, J. N. 2010 High-concentration, surfactant-stabilized graphene dispersions. *ACS Nano* **4** (6), 3155–3162.

MANDAL, S., BANDOPADHYAY, A. & CHAKRABORTY, S. 2016a Dielectrophoresis of a surfactant-laden viscous drop. *Phys. Fluids* **28** (6), 062006.

MANDAL, S. & CHAKRABORTY, S. 2017 Influence of interfacial viscosity on the dielectrophoresis of drops. *Phys. Fluids* **29** (5), 052002.

MANDAL, S., DAS, S. & CHAKRABORTY, S. 2017 Effect of Marangoni stress on the bulk rheology of a dilute emulsion of surfactant-laden deformable droplets in linear flows. *Phys. Rev. Fluids* **2** (11), 113604.

MANDAL, S., GHOSH, U. & CHAKRABORTY, S. 2016b Effect of surfactant on motion and deformation of compound droplets in arbitrary unbounded Stokes flows. *J. Fluid Mech.* **803**, 200–249.

MANIKANTAN, H. & SQUIRES, T. M. 2020 Surfactant dynamics: hidden variables controlling fluid flows. *J. Fluid Mech.* **892**, P1.

MAULEON-AMIEVA, A., ALLEN, M. P., LIVERPOOL, T. B. & ROYALL, C. P. 2023 Dynamics and interactions of quincke roller clusters: From orbits and flips to excited states. *Sci. Adv.* **9** (20), eadf5144.

McDOUGALL, M. A., WILSON, S. K. & DAS, D. 2025 Nonlinear three-dimensional electrohydrodynamic interactions of viscous dielectric drops. *arXiv preprint arXiv:2505.10986*.

MILLIKEN, W. J. & LEAL, L. G. 1994 The influence of surfactant on the deformation and breakup of a viscous drop: The effect of surfactant solubility. *J. Colloid Interface Sci.* **166** (2), 275–285.

MILLIKEN, W. J., STONE, H. A. & LEAL, L. G. 1993 The effect of surfactant on the transient motion of Newtonian drops. *Phys. Fluids* **5** (1), 69–79.

MOODY, C. A. & FIELD, J. A. 2000 Perfluorinated surfactants and the environmental implications of their use in fire-fighting foams. *Environ. Sci. & Technol.* **34** (18), 3864–3870.

NAWAB, M. A. & MASON, S. G. 1958 The viscosity of dilute emulsions. *Trans. Faraday Soc.* **54**, 1712–1723.

NGANGUIA, H., DAS, D., PAK, O. S. & YOUNG, Y.-N. 2023 Influence of surface viscosities on the electrodeformation of a prolate viscous drop. *Soft Matter* **19** (4), 776–789.

NGANGUIA, H., PAK, O. S. & YOUNG, Y.-N. 2019 Effects of surfactant transport on electrodeformation of a viscous drop. *Phys. Rev. E* **99** (6), 063104.

NGANGUIA, H., YOUNG, Y.-N., VLAHOVSKA, P. M., BLAWZDZIEWICZ, J., ZHANG, J. & LIN, H. 2013 Equilibrium electro-deformation of a surfactant-laden viscous drop. *Phys. Fluids* **25** (9), 092106.

O'KONSKI, C. T. & THACHER, H. C. 1953 The distortion of aerosol droplets by an electric field. *J. Phys. Chem.* **57**, 955–958.

OLIVEIRA, M. S. N., PINHO, F. T., POOLE, R. J., OLIVEIRA, P. J. & ALVES, M. A. 2009 Purely elastic flow asymmetries in flow-focusing devices. *J. Non-Newton. Fluid Mech.* **160** (1), 31–39.

PAN, X.-D. & MCKINLEY, G. H. 1997 Characteristics of electrorheological responses in an emulsion system. *J. Colloid Interface Sci.* **195** (1), 101–113.

PAWAR, Y. & STEBE, K. J. 1996 Marangoni effects on drop deformation in an extensional flow: The role of surfactant physical chemistry. I. Insoluble surfactants. *Phys. Fluids* **8** (7), 1738–1751.

PENG, G. G., BRANDÃO, R., YARIV, E. & SCHNITZER, O. 2024 Equatorial blowup and polar caps in drop electrohydrodynamics. *Phys. Rev. Fluids* **9** (8), 083701.

PENG, G. G. & SCHNITZER, O. 2025 Bistability and charge-density blowup in the onset of drop Quincke rotation. *Phys. Rev. Fluids* **10** (8), 081701.

PODDAR, A., MANDAL, S., BANDOPADHYAY, A. & CHAKRABORTY, S. 2018 Sedimentation of a surfactant-laden drop under the influence of an electric field. *J. Fluid Mech.* **849**, 277–311.

PODDAR, A., MANDAL, S., BANDOPADHYAY, A. & CHAKRABORTY, S. 2019a Electrical switching of a surfactant coated drop in poiseuille flow. *J. Fluid Mech.* **870**, 27–66.

PODDAR, A., MANDAL, S., BANDOPADHYAY, A. & CHAKRABORTY, S. 2019b Electrorheology of a dilute emulsion of surfactant-covered drops. *J. Fluid Mech.* **881**, 524–550.

POOLE, R. J. 2023 Inelastic and flow-type parameter models for non-newtonian fluids. *J. Non-Newton. Fluid Mech.* **320**, 105106.

QUINCKE, G. 1896 Ueber Rotationen im constanten elektrischen Felde. *Ann. Phys. Chem.* **295** (11), 417–486.

RAJU, G., KYRIAKOPOULOS, N. & TIMONEN, J. V. I. 2021 Diversity of non-equilibrium patterns and emergence of activity in confined electrohydrodynamically driven liquids. *Sci. Adv.* **7** (38), eabh1642.

REYES GARZA, R., KYRIAKOPOULOS, N., CENEV, Z. M., RIGONI, C. & TIMONEN, J. V. I. 2023 Magnetic Quincke rollers with tunable single-particle dynamics and collective states. *Sci. Adv.* **9** (26), eadh2522.

RISTENPART, W. D., BIRD, J. C., BELMONTE, A., DOLLAR, F. & STONE, H. A. 2009 Non-coalescence of oppositely charged drops. *Nature* **461** (7262), 377–380.

ROSEN, M. J. & KUNJAPPU, J. T. 2012 *Surfactants and interfacial phenomena*. John Wiley & Sons.

RUMSCHEIDT, F. D. & MASON, S. G. 1961 Particle motions in sheared suspensions XII. Deformation and burst of fluid drops in shear and hyperbolic flow. *J. Colloid Sci.* **16** (3), 238–261.

SADHAL, S. S. & JOHNSON, R. E. 1983 Stokes flow past bubbles and drops partially coated with thin films. Part 1. Stagnant cap of surfactant film—exact solution. *J. Fluid Mech.* **126**, 237–250.

SADHAL, S. S. & JOHNSON, R. E. 1986 On the deformation of drops and bubbles with varying interfacial tension. *Chem. Eng. Commun.* **46** (1-3), 97–109.

SALIPANTE, P. F. & VLAHOVSKA, P. M. 2010 Electrohydrodynamics of drops in strong uniform dc electric fields. *Phys. Fluids* **22** (11), 112110.

SALIPANTE, P. F. & VLAHOVSKA, P. M. 2013 Electrohydrodynamic rotations of a viscous droplet. *Phys. Rev. E* **88** (4), 043003.

SAVIC, P. 1953 Circulation and distortion of liquid drops falling through a viscous medium. *Tech. Rep. MT-22*. Division of Mechanical Engineering, National Research Council Canada.

SCRIVEN, L. E. 1960 Dynamics of a fluid interface equation of motion for newtonian surface fluids. *Chem. Eng. Sci.* **12** (2), 98–108.

SHERWOOD, J. D. 1988 Breakup of fluid droplets in electric and magnetic fields. *J. Fluid Mech.* **188**, 133–146.

SHKADOV, V. Y. & SHUTOV, A. A. 2002 Drop and bubble deformation in an electric field. *Fluid Dyn.* **37** (5), 713–724.

SHUTOV, A. A. 2002 The shape of a drop in a constant electric field. *Tech. Phys.* **47**, 1501–1508.

SORGENTONE, C., TORNBERG, A.-K. & VLAHOVSKA, P. M. 2019 A 3D boundary integral method for the electrohydrodynamics of surfactant-covered drops. *J. Comput. Phys.* **389**, 111–127.

STONE, H. A. 1990 A simple derivation of the time-dependent convective-diffusion equation for surfactant transport along a deforming interface. *Phys. Fluids* **2** (1), 111–112.

STONE, H. A. & LEAL, L. G. 1990 The effects of surfactants on drop deformation and breakup. *J. Fluid Mech.* **220**, 161–186.

SUPEENE, G., KOCH, C. R. & BHATTACHARJEE, S. 2008 Deformation of a droplet in an electric field: Nonlinear transient response in perfect and leaky dielectric media. *J. Colloid Interface Sci.* **318** (2), 463–476.

TAYLOR, G. I. 1932 The viscosity of a fluid containing small drops of another fluid. *Proc. R. Soc. Lond. A* **138** (834), 41–48.

TAYLOR, G. I. 1934 The formation of emulsions in definable fields of flow. *Proc. R. Soc. Lond. A* **146** (858), 501–523.

TAYLOR, G. I. 1964 Disintegration of water drops in an electric field. *Proc. R. Soc. Lond. A* **280** (1382), 383–397.

TAYLOR, G. I. 1966 Studies in electrohydrodynamics. I. The circulation produced in a drop by an electric field. *Proc. R. Soc. Lond. A* **291** (1425), 159–166.

TEIGEN, K. E. & MUNKEJORD, S. T. 2010 Influence of surfactant on drop deformation in an electric field. *Phys. Fluids* **22** (11), 112104.

TORZA, S., COX, R. G. & MASON, S. G. 1971 Electrohydrodynamic deformation and bursts of liquid drops. *Philos. Trans. R. Soc. Lond. A* **269** (1198), 295–319.

TURCU, I. 1987 Electric field induced rotation of spheres. *J. Phys. A: Math. Gen.* **20** (11), 3301–3307.

VAISMAN, L., WAGNER, H. D. & MAROM, G. 2006 The role of surfactants in dispersion of carbon nanotubes. *Adv. Colloid Interface Sci.* **128**, 37–46.

VIZIKA, O. & SAVILLE, D. A. 1992 The electrohydrodynamic deformation of drops suspended in liquids in steady and oscillatory electric fields. *J. Fluid Mech.* **239**, 1–21.

VLAHOVSKA, P. M. 2011 On the rheology of a dilute emulsion in a uniform electric field. *J. Fluid Mech.* **670**, 481–503.

VLAHOVSKA, P. M., LOEWENBERG, M. & BLAWZDZIEWICZ, J. 2005 Deformation of a surfactant-covered drop in a linear flow. *Phys. Fluids* **17** (10), 103103.

WEILER, W. 1893 Zur darstellung elektrischer kraftlinien. *Z. Phys. Chem. Unterricht* **6**, 194–195.

ZHANG, J., LIU, H. & ZHANG, X. 2021a Modeling the deformation of a surfactant-covered droplet under the combined influence of electric field and shear flow. *Phys. Fluids* **33** (4), 042109.

ZHANG, Z., YUAN, H., DOU, Y., DE LA CRUZ, M. O. & BISHOP, K. J. M. 2021b Quincke oscillations of colloids at planar electrodes. *Phys. Rev. Lett.* **126** (25), 258001.